N71-36352

NASA CR-72977

HYBRID AND DECOMPOSITION COMBUSTION OF THE HYDRAZINE FUELS

by

C.B. Allison

Mechanical Engineering Department
The Pennsylvania State University
University Park, Pennsylvania

prepared for

NATIONAL AERONAUTICS AND SPACE ADMINISTRATION

NASA Lewis Research Center
Contract NGR 39-009-077
Richard J. Priem, Program Manager and Technical Monitor

1. Report No. CR 72977	2. Government Accession No.	3. Recipient's Catalog No.

4. Title and Subtitle

HYBRID AND DECOMPOSITION COMBUSTION OF THE HYDRAZINE FUELS

5. Report Date
July 1971

6. Performing Organization Code

7. Author(s)
C. B. Allison

8. Performing Organization Report No.

9. Performing Organization Name and Address
Mechanical Engineering Department
The Pennsylvania State University
University Park, Pennsylvania 16802

10. Work Unit No.

11. Contract or Grant No.
NGR 39-009-077

12. Sponsoring Agency Name and Address
National Aeronautics and Space Administration
Washington, D. C. 20546

13. Type of Report and Period Covered
Contractor Report

14. Sponsoring Agency Code

15. Supplementary Notes

Program Manager and Technical Monitor, Richard J. Priem, Chemical Rocket Division, NASA Lewis Research Center, Cleveland, Ohio

16. Abstract

The combustion characteristics of the hydrazine fuels (N_2H_4, MMH, and UDMH) were studied for both oxidation (hybrid combustion) and decomposition conditions. A flat flame burner was used to provide the high temperature gaseous environment for burning drops of liquid fuel at atmospheric pressure. The burner provided a temperature range of 1660 K to 2530 K and an ambient oxygen mass fraction range of 0.0 to 0.42. In addition, a wide range of drop sizes (0.11 cm to 1.91 cm) were considered by employing both the porous sphere and suspended droplet experimental techniques. It was found that the burning rates of all three fuels increased with increasing drop diameter, ambient temperature, and ambient oxygen concentration. To aid in correlating the data obtained, a theoretical hybrid combustion model was developed. This model was applied to the present data as well as other data on hydrazine fuel combustion available in the literature. The average error between predicted burning rates using the model and measured burning rates was less than 20% for all three fuels.

17. Key Words (Suggested by Author(s))
Hydrazine fuel combustion
Hybrid
Decomposition

18. Distribution Statement
Unclassified - Unlimited

19. Security Classif. (of this report) Unclassified	20. Security Classif. (of this page) Unclassified	21. No. of Pages 105	22. Price* $3.00

* For sale by the National Technical Information Service, Springfield, Virginia 22151

FOREWARD

This report summarizes a portion of the work done on NASA Grant NGR 39-009-077. The study was under the direction of G. M. Faeth, Associate Professor of Mechanical Engineering.

TABLE OF CONTENTS

LIST OF TABLES

LIST OF FIGURES

LIST OF FIGURES (CONTINUED)

NOMENCLATURE

Symbol	Description
A	Pre-exponential factor, Equation (3.43), gm/cm^2-sec
$B_1, \ldots, B_6$	Constants in property equations, Appendix A
C	Specific heat at constant pressure, cal/gm-K
D	Binary diffusion coefficient, cm^2/sec
d_ℓ	Drop diameter, cm
E	Activation energy, Equation (3.43), kcal/mole
Gr	Grashof number
g	Acceleration of gravity, cm/sec^2
ΔH°	Standard heat of formation at T°, cal/gm
h	Enthalpy, cal/gm
K	Evaporation constant, cm^2/sec
L	Heat of vaporization, cal/gm
Le	Lewis number
L^*	Nondimensional heat of vaporization, Equation (3.31)
ℓ_1, ℓ_2	Major and minor diameters, respectively, Equation (2.1), cm
M_i	Molecular weight of species i, gm/mole
$\dot{M}$	Total mass flow rate, gm/sec
$\dot{M}^*$	Total mass flow rate for no convection effects, gm/sec
$\dot{m}$	Mass flow rate per unit solid angle, gm/sec
N	Total number of species
Nu	Nusselt number
Nu*	Nusselt number for no flow conditions

NOMENCLATURE (CONTINUED)

Symbol	Description
P	Pressure, atm
Pr	Prandtl number
Q_1	Parameter, Equation (3.32)
Q_2	Parameter, Equation (3.33)
q_1	Parameter, Equation (3.19), cal/gm
q_2	Parameter, Equation (3.20), cal/gm
R	Universal gas constant, cal/mole-K
Re	Reynolds number
r	Radial distance, cm
T	Temperature, K
T°	Reference temperature, K
U_i	Diffusion velocity of species i, cm/sec
V_∞	Velocity of the ambient gas, cm/sec
v	Mass average velocity, cm/sec
X_i	Mole fraction of species i
Y_i	Mass fraction of speices i
β	Dimensionless radial distance, Equation (3.29)
ε_i	Mass flux fraction of species i
γ	Stoichiometric coefficient
λ	Thermal conductivity, cal/cm-sec-K
μ	Viscosity, gm/cm-sec
ρ	Density, gm/cm^3
σ	Parameter, Equation (3.24), cal/gm-K
θ	Dimensionless temperature

NOMENCLATURE (CONTINUED)

Symbol	Description
Subscripts	
A	Region A
B	Region B
C	Region C
d	Critical point
F	Fuel
FP	Fuel decomposition products
f	Bipropellant flame
I	Monopropellant flame
i	Species i
j	Region j
ℓ	Droplet surface
O	Oxidizer
P	Bipropellant flame products
∞	Ambient conditions
Superscripts	
$\circ$	Reference conditions
$+$	Outer side of a surface
$-$	Inner side of a surface

SUMMARY

The major objective of the present study was to investigate the combustion characteristics of the hydrazine fuels in the form of liquid drops at atmospheric pressure. Particular emphasis was placed on high ambient temperature conditions representative of combustion chambers. The burning rates (gm/sec) of hydrazine, MMH, and UDMH as a function of drop diameter, ambient temperature, and ambient oxygen concentration were obtained. Aerozine 50 was also tested. However, a stable burning condition could not be achieved with Aerozine 50 for any test condition.

The hydrazine fuels are capable of exothermic decomposition and may be employed as monopropellants as well as the fuel component of a bipropellant system. Hybrid combustion, i.e., the burning of a monopropellant in an oxidizing medium, has some of the characteristics of both monopropellant and bipropellant combustion. Another objective of the study was to develop a hybrid combustion theoretical model to correlate the data obtained.

The high ambient temperatures and various ambient oxygen concentrations were obtained by placing drops of liquid fuel directly in the combustion products of a flat flame burner. The burner provided a temperature range of 1660 K to 2530 K and ambient oxygen mass fractions in the range of 0.0 to 0.42.

In order to obtain a wide range of drop diameters (0.11 cm to 1.91 cm), two techniques were employed for burning rate measurements. The larger drop sizes were simulated by a porous alundum sphere.

Liquid propellant was fed to the center of the sphere through a water cooled tube; the burning rate was measured directly from the propellant feed rate. Suspended droplets were employed for testing the smaller drop sizes. Plots of droplet diameter variation with time yielded the burning rate during steady combustion.

To aid in correlating the data, a hybrid combustion model was developed. In this model the inner decomposition flame was assumed to be infinitely thin. The radial position of this inner flame was assumed to be located at the point where the unreacted gas flows into the flame surface at the laminar burning velocity of the mixture. The bipropellant reaction was assumed to be infinitely fast so that kinetic effects could be ignored. The equations developed with this model are such that they correctly reduce to the limiting cases of pure monopropellant combustion, pure bipropellant combustion, and evaporation with no combustion.

The experimental mass burning rates increased with increasing drop diameter, ambient temperature, and ambient oxygen concentration. As drop diameter increased the influence of ambient conditions (temperature, oxygen concentration, convection) decreased. In addition, as drop diameter increased the experimental mass burning rates deviated from a bipropellant solution. This was particularly true for hydrazine where experimental data was as much as an order of magnitude greater than the non-reactive theory predictions.

The hybrid theory predicted burning rates in good agreement with experimental values throughout the test range. This model was used to predict the present data plus data on hydrazine

combustion available in the literature. Taken together, the hybrid theory gave good predictions for burning rates varying over two orders of magnitude for each of the three fuels, for a wide variety of droplet sizes (0.038 cm to 1.91 cm in diameter) and ambient conditions (300-2530 K, oxygen concentrations of 0 to 100%, pressures from 1 atm to 7.8 atm). The average error between predicted and experimental values was less than 20% for all three fuels.

CHAPTER I

INTRODUCTION

1.1 General Statement of the Problem

Liquid fuel combustion is an important field of study of combustion phenomena. Many devices such as diesel engines, gas turbines, home oil heaters, and liquid rocket engines involve the combustion of a liquid fuel. These devices burn liquid droplets in a gas; this process is called spray combustion.

Prerequisite to the understanding of spray combustion is the understanding of the combustion process for an individual drop. Droplet studies form the foundation for the prediction of steady state combustion chamber performance. In addition, the model most widely used to predict combustion instability in liquid fueled rocked engines requires the knowledge of individual droplet combustion characteristics. (1)*

Droplet combustion can be broken down into three major subdivisions: bipropellant combustion, monopropellant combustion, and hybrid combustion. Bipropellant combustion is characterized by a diffusion flame. The fuel vaporizes from the surface of the drop and diffuses radially outward to a flame zone which surrounds the droplet. The oxidizer diffuses into this flame zone from the ambient gas. A monopropellant is capable of exothermic decomposition

---

*Numbers in parenthesis refer to items in the Bibliography.

and can support a flame front around the droplet in the absence of an oxidizing medium. Hybrid combustion, the burning of a monopropellant in an oxidizing medium, exhibits some of the characteristics of both monopropellant and bipropellant combustion. The fuel vaporizes from the liquid surface and undergoes exothermic decomposition. The decomposition products diffuse radially outward and at some point react with the oxidizing medium.

Monopropellant and bipropellant droplet combustion has received a great deal of attention in the literature, however, there have been relatively few studies on hybrid combustion. A common hybrid system involves the monopropellant, hydrazine, N_2H_4, and several of its derivatives (monomethylhydrazine, unsymmetrical dimethylhydrazine) with oxidizers in rocket propulsion systems. For example, the Apollo command module thruster, and the lunar ascent and descent engines employ hydrazine fuels. The topic of the present investigation was the hybrid combustion of hydrazine fuels, in view of this practical importance.

1.2 Previous Related Studies

Liquid fuel droplet combustion is characterized by two regimes during the droplet lifetime: the preheat and steady burning regimes. The major difference between these regimes is that the liquid temperature rises during the preheat regime but remains constant during the steady burning regime.

During the preheat period, a portion of the energy reaching the droplet surface is used for sensible heating of the liquid. The remaining portion of the energy is used for vaporization. With increasing droplet temperature, the rate of vaporization increases. Eventually the droplet reaches a condition where all the energy reaching the droplet surface is used to vaporize the liquid. This signals the onset of the steady burning regime.

During steady burning the droplet temperature remains constant at its so-called "wet bulb temperature." Only the steady burning regime is considered in the present work.

Numerous studies have been conducted on the vaporization and combustion of liquid droplets. Only those studies involving the hydrazine propellants are discussed in the following.

Rosser (2) conducted a study on hydrazine combustion using a porous sphere to simulate a droplet. Fuel was supplied internally to the sphere and forced radially outward from the center by a motor driven syringe pump. The fuel burned as it reached the sphere surface. The mass flow of fuel supplied was a direct measure of the burning rate.

Sphere sizes in the range of 3-13 mm in diameter were used in the experiments of Reference (2). The ambient oxygen concentration was varied by placing the porous sphere in a closed container and passing a mixture of oxygen and nitrogen slowly upward past the burning sphere. Hydrazine of about 97-98% purity containing approximately 1.5% by weight of water and aniline was used in the tests.

At atmospheric pressure, Rosser found that 8-10% by volume of oxygen was required to maintain a stable flame surrounding the sphere. For oxygen concentrations greater than 10%, a double flame characteristic of hybrid combustion was observed. Rosser attributed this double flame to a decomposition flame of hydrazine surrounded by an oxidation flame of the decomposition products. This double flame was stable for all oxygen concentrations tested greater than 10%.

For the hydrazine decomposition flame (10% O_2-90% N_2, by volume, by Rosser's definition), the mass burning rate per unit area was constant over the entire range of sphere sizes and equal to 0.014 gm/cm^2-sec. (2) The mass burning rate for double flame conditions was consistently greater than the mass burning rate for decomposition burning.

Rosser and Peskin (3) extended the previous work of Rosser (2). Hydrazine of different purity was used; pressures were extended to less than 1 atm. They found that hydrazine containing about 0.5% aniline and 1.5% water by weight could support a decomposition flame in the absence of oxygen at atmospheric pressure but not at lower pressures. This is in contrast to Rosser's (2) work with hydrazine of 1.5% aniline concentration. The hydrazine with lower aniline concentration had a 45% greater burning rate; adding aniline reduced the burning rate to the values obtained with the 1.5% aniline concentration hydrazine. For both hydrazines tested, a double flame was observed with ambient oxygen concentrations greater than 10% by volume.

Del Notario and Tarifa (4) studied hydrazine combustion for drops somewhat smaller than used by Rosser (2). They suspended drops (on the order of 1-2 mm in diameter) of hydrazine (98% purity) from a quartz fiber. A furnace with a fixed proportion of oxygen was then raised to surround the drop. The variation of drop diameter with time was recorded photographically. The slope of the curve of diameter squared with time, called the burning rate or the evaporation constant (cm^2/sec), was obtained from these measurements. Pressure was maintained constant at 1 atm; temperature was varied from about 400-1000 C.

Del Notario found that in every case a small proportion of oxygen was required to maintain combustion. In a pure nitrogen environment the evaporation constant increased slightly with temperature. The evaporation constant also increased with increasing ambient oxygen concentration.

The results of del Notario and Tarifa are in question due to radiation from the furnace walls to the liquid phase. Faeth, et al., (5) found that furnace wall radiation contributed significantly to droplet evaporation at temperatures above 800 K at atmospheric pressure.

Dykema and Greene (6) also suspended small droplets from a quartz fiber. In addition to hydrazine they burned unsymmetrical dimethylhydrazine (UDMH) in air and in 100% oxygen at room temperature and atmospheric pressure. The variation of drop diameter with time was recorded photographically. They report an evaporation constant of 0.016 cm^2/sec in air and 0.035 cm^2/sec in pure oxygen for hydrazine. For UDMH they found a burning rate of 0.011 cm^2/sec in air and 0.030 cm^2/sec in oxygen.

Lawver (7) suspended hydrazine drops from a 0.01 inch chromel alumel thermocouple in an atmosphere of pure nitrogen tetroxide at about 150 F. To simulate the combustion environment of a rocket engine combustion chamber, he also suspended one droplet directly in the high temperature combustion products of another droplet.

For hydrazine drops burning in pure nitrogen tetroxide, the mass burning rate per unit area did not reach a constant value before burnout. For a droplet burning in the combustion gases of another droplet, the mass burning rate reached a constant value of 0.061 g/cm^2-sec. (7)

Lawver, Kosvic, and Breen (8) suspended hydrazine and UDMH fuel droplets from a water cooled needle. Drop diameter was maintained constant using a motor driven syringe pump. The droplets were burned in pure nitrogen tetroxide vapor and in mixtures of oxygen and nitrogen at atmospheric pressure and approximately room temperature. They found that the mass burning rate of hydrazine burning in N_2O_4 vapor increased linearly with drop diameter; however, the mass burning rate of hydrazine burning in air varied as drop diameter to a power greater than one.

In a later work by Kosvic and Breen (9), the results for hydrazine were extended to pressures greater than one atmosphere. For this study, Kosvic and Breen used a free drop burner. A hydrazine/nitrogen tetroxide gas generator was employed to provide the ambient atmosphere to the drop. Hydrazine, in the form of liquid drops, was added to the combustion products of the gas generator. By measuring the size variations of the drop photographically, burning rates were determined.

The experimental apparatus of Reference (9) was constructed to provide a pressure range of 1.0 to 34 atmospheres, a velocity of 1 to 100 ft/sec, and a temperature of 1000 to 5500 F. However, only a limited amount of data was taken due to problems encountered in the apparatus. For the results presented, the mass burning rate appears to vary linearly with drop diameter at a pressure of 7.8 atm. The ambient temperature and gas velocity were not specified, however, for this test condition.

As indicated by the preceding discussion, a number of investigators have studied hydrazine type fuel combustion. All have observed the phenomena associated with hybrid type fuel combustion at low temperature. Kosvic and Breen (9) undertook a novel approach to determine fuel burning rates at high temperature and high pressure. However, their reported data is quite limited and experimental conditions are not well defined.

Hybrid combustion is more difficult to treat theoretically than either pure monopropellant or pure bipropellant combustion. Bipropellant combustion theory has been fairly successful in predicting experimental burning rates. Monopropellant theory has not been quite as successful mainly because of the difficulty in treating kinetic effects. Incorporating kinetics into the theoretical developments is not an easy task and can only be accomplished for limiting cases. The analysis of hybrid combustion, a combination of bipropellant and monopropellant effects, also involves the same difficulties with kinetics but with the additional complication of the oxidation flame. Various theories on monopropellant combustion are discussed in the section titled Theoretical Considerations.

1.3 Specific Statement of the Problem

The preceding discussion has indicated the need for further investigation of hybrid combustion, particularly at conditions representative of those found in a combustion chamber. Since propellant vaporization is an important parameter used to predict steady state combustion chamber performance, experimental values of droplet burning rates at high temperature are of considerable importance. The existing data is either in question due to radiation effects, del Notario and Tarifa (4), or of limited usefulness because of undefined experimental conditions, Lawver (7) and also Kosvic and Breen (9).

Therefore, the present work considered the combustion of hydrazine type fuel droplets with the following objectives:

1. Determine quantitative values of droplet burning rates as a function of ambient temperature and ambient oxygen concentration for temperatures approximating those in a liquid rocket engine combustion chamber, at atmospheric pressure.
2. Measure the effect of droplet diameter on droplet burning rate.
3. Qualitatively investigate the hybrid combustion, two flame, phenomena at high temperature.

4. Determine if a semitheoretical correlation of hybrid combustion can predict the data obtained.

The specific fuels considered in the study were hydrazine (N_2H_4), monomethylhydrazine (MMH), unsymmetrical dimethylhydrazine (UDMH), and Aerozine 50 (denoted A-50 consisting of 50% N_2H_4 and 50% UDMH by weight).

CHAPTER II

APPARATUS

2.1 Flat Flame Burner

A flat flame burner apparatus was employed to provide the high temperature ambient gas around the test droplet. The tests were limited to atmospheric pressure; however, by changing the mixture ratio of the burner a variety of ambient oxygen concentrations could be considered.

Both the suspended droplet and porous sphere techniques were employed to experimentally determine droplet burning rates. For the suspended droplet method, droplets were supported from a quartz fiber and photographed as they burned. Analysis of the droplet diameter variation as a function of time then yielded the burning rate. The porous sphere method consisted of supplying fuel continuously to the center of the porous sphere during the combustion process. The fuel feed rate, where the sphere remained fully wetted without dripping, then yielded the burning rate directly.

Eastman Organic fuels were used in the testing: hydrazine (95+ % purity), MMH (boiling point 87-88 C), and UDMH (boiling point 61-63 C). Aerozine 50, a mixture of 50% hydrazine and 50% UDMH by weight, was blended from these fuels. Some testing was conducted using analyzed UDMH (99.8% purity) supplied by the FMC Corporation.

A flat flame burner developed by Faeth (10) was employed in the testing. A sketch of this apparatus is shown in Figure 1. In

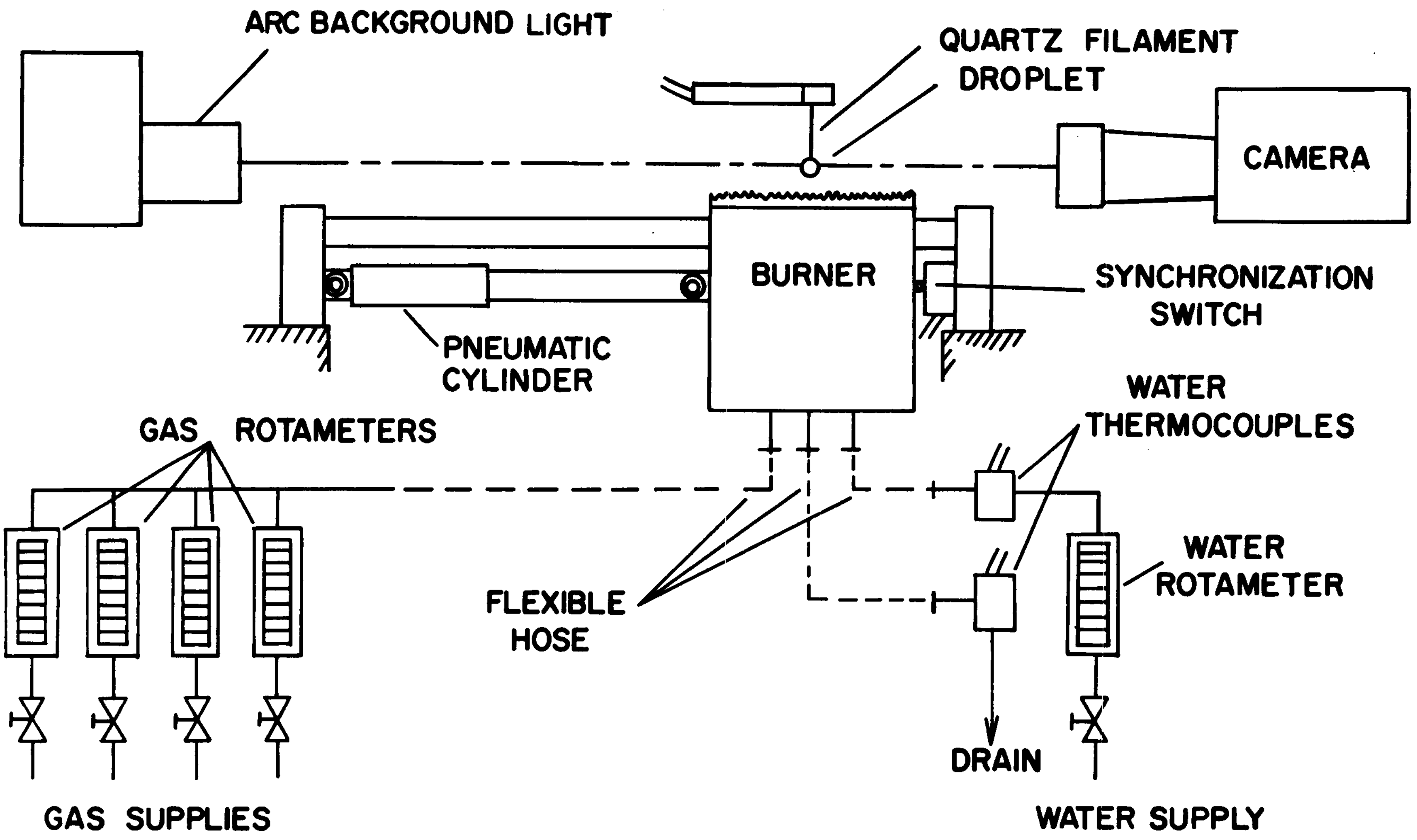

Figure 1 Schematic Diagram of the Flat Flame Burner Apparatus

order to rapidly immerse the test droplet in the burner combustion products, the burner was mounted on rails and moved with a solenoid valve actuated pneumatic cylinder. A high speed motion picture camera was used to measure the time between the droplet first entering the burner flame and the burner coming to rest in the test position. This time was found to be on the order of 10 msec.

The burner itself was similar to the one described by Friedman and Macek (11). The burner face consisted of a porous bronze disk, 5 cm in diameter, cooled on its lower surface at a series of points by contact with a water cooled copper block. The flow rate of the cooling water was measured using a rotameter. The temperature rise of the cooling water was measured with chromel-alumel thermocouples. The heat loss from the flame to the burner was calculated from the measured flow rate and temperature rise of the cooling water.

Various mixtures of carbon monoxide (technical grade), oxygen, and nitrogen (commercial grade) were used to provide ambient oxygen concentrations in the range of 0-42% by mass and temperatures in the range of 1660-2530 K. Rotameters calibrated with a wet test meter were used to measure the flow rate of the gases. Hydrogen was also used to determine the effect of water vapor on the burning rate at several temperatures.

The temperatures and composition of the product combustion gas of the burner were calculated allowing for all relevant dissociation reactions and the experimentally determined heat loss to the burner face. The thermochemical properties required for these calculations were taken from the JANAF Tables (12).

The gas velocity at the droplet location was calculated from the mass flux into the burner and the known properties of the burned gas. This approach is sufficiently accurate since the test position was well within the potential core of the jet leaving the burner.

Table 1 summarizes the computed properties of the gas stream at the droplet location for the test conditions used. The ambient oxygen mass fraction is an effective value based on concentrations of possible oxidizing species (O_2, O, NO). Product species with concentrations less than 0.1% are not listed in Table 1. These minor species were used, however, in calculating ambient oxygen mass fractions, ambient temperatures, and velocities at the droplet location.

2.2 Suspended Droplet Technique

For the suspended droplet tests, the droplets were mounted on a quartz filament approximately 100μ in diameter. The bottom end of the filament was slightly enlarged to aid in supporting the droplet. Droplet diameters were measured from shadowgraphs recorded by a 16 mm cine camera operating at speeds on the order of 100 frames per second. The background light was provided by a mercury arc lamp. Timing marks were placed on the edge of the film by an internal timing light powered by a 100 cps pulse generator. Kodak Plus-X Reversal film, developed as a negative, was used in the testing.

The preliminary setup for a series of tests at a given test condition involved focussing the camera, pressurizing the supply tank to operate the pneumatic cylinder, and regulating the supply

Table 1

Properties of the Ambient Gas from the Flat Flame Burner for Various Test Conditions

$Y_{O\infty}$	T_∞ (K)	V_∞ (cm/sec)	Product Mole Fraction							
			CO	CO_2	NO	N_2	O	O_2	H_2	H_2O
.043	2530	53.4	.098	.478	.008	.370	.003	.043	0	0
.132	2530	53.4	.050	.436	.014	.358	.006	.137	0	0
.233	2530	53.4	.038	.450	.015	.237	.008	.252	0	0
.328	2530	53.4	.031	.446	.014	.136	.010	.362	0	0
.418	2530	53.4	.027	.440	.009	.042	.011	.471	0	0
0	2470	55.7	.291	.421	0	.284	0	0	0	0
0	2330	55.7	.251	.373	0	.374	0	0	0	0
0	2255	55.7	.223	.333	0	.444	0	0	0	0
0	2165	55.7	.200	.300	0	.500	0	0	0	0
0	2060	55.7	.182	.273	0	.545	0	0	0	0
0	1935	55.7	.429	.286	0	.286	0	0	0	0
0	1835	55.7	.375	.250	0	.375	0	0	0	0
0	1750	55.7	.333	.222	0	.444	0	0	0	0
0	1660	55.7	.300	.200	0	.500	0	0	0	0
0	1835	63.8	.315	.375	0	.138	0	0	.030	.142
0	1750	63.8	.283	.342	0	.219	0	0	.029	.127
0	1660	63.8	.306	.306	0	.306	0	0	.028	.111

gases and cooling water. After igniting the gas mixture from the burner, the flame was allowed to stabilize for a sufficient period of time.

The droplet was then mounted on the quartz filament with a glass syringe and a cycling timer was actuated. The electrically driven motion picture camera was started and allowed to reach operating speed. The solenoid valve was then actuated and the pneumatic cylinder forced the burner under the droplet. The droplet ignited and burned for approximately 2 seconds. The solenoid valve was then de-energized allowing the burner to return to its original position. The camera power was turned off to complete the test cycle.

The films obtained were analyzed using a Vanguard Motion Picture Analyzer which was calibrated by photographing a wire of known size at the droplet location. The elliptical shape of the droplet was corrected to a sphere having the same volume using the method of Kobayasi (13). The diameter of the equivalent sphere, taken to be the drop diameter, was given by the formula

$$d_{\ell} = (\ell_1 \ell_2^2)^{1/3} \tag{2.1}$$

where ℓ_1 and ℓ_2 are the major and minor diameters, respectively, of the elliptically shaped droplet.

2.3 Porous Sphere Technique

To determine the effect of drop diameter on the burning rate for the fuels tested, a porous sphere technique similar to that used by Rosser (2) was employed. As shown in Figure 2, fuel was supplied internally to the porous sphere. The fuel was forced radially

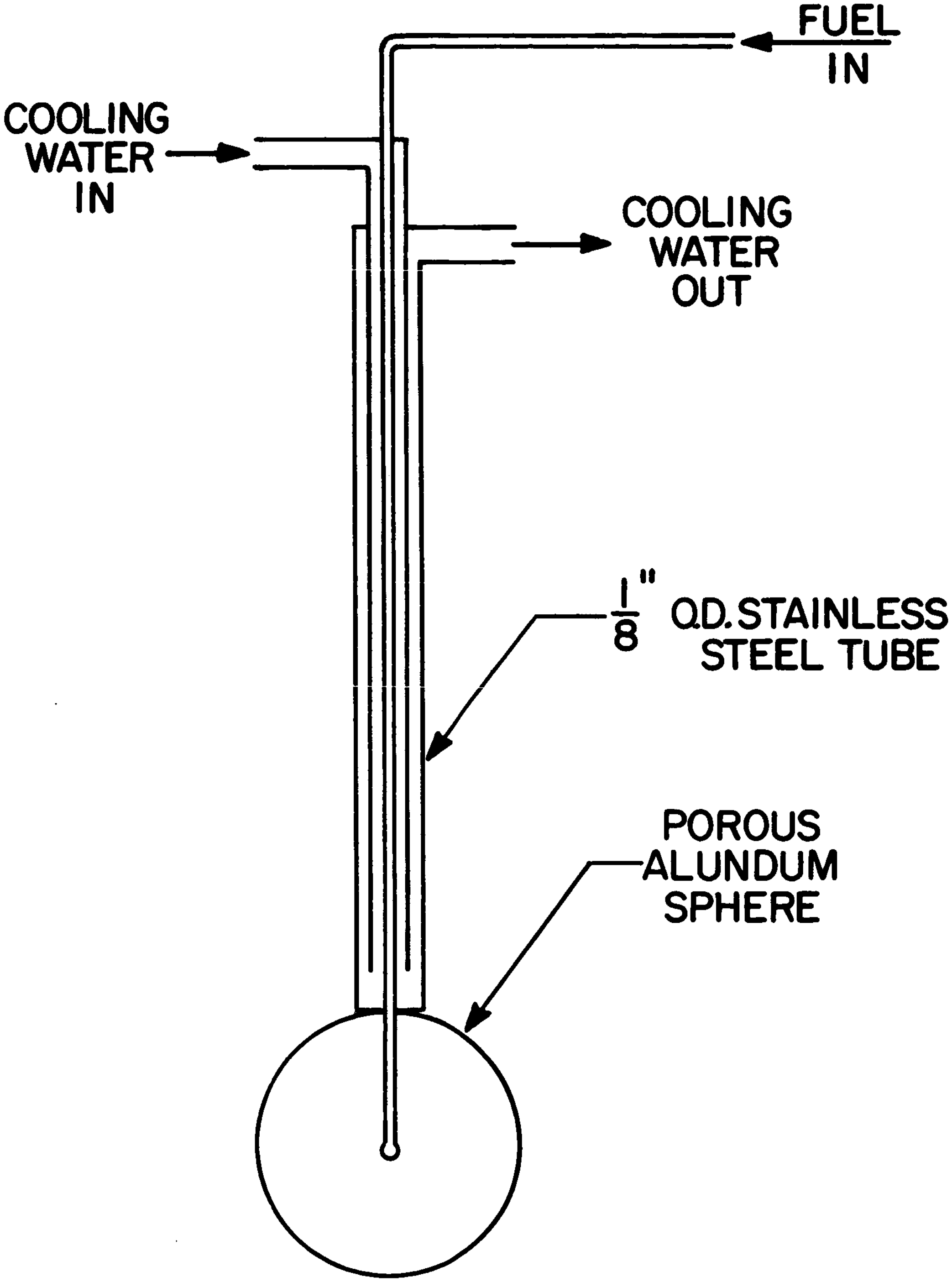

Figure 2 Sketch of the Porous Sphere Probe

outward and burned as it reached the sphere surface. The fuel flow rate was monitored using a Sage syringe pump which was calibrated by measuring the volume flow of liquid as a function of pump setting.

Calculations indicated the need for a means of cooling the inflowing fuel to the porous sphere since the feed tube was surrounded by high temperature gases. This was accomplished by using the cooling manifold shown in Figure 2. Thermocouples were mounted at the inlet and outlet of the cooling manifold; the temperature rise of the cooling water was continuously monitored throughout the testing and never exceeded 2 F.

The porous alundum spheres were obtained from the Norton Company. Manufacturing irregularities in the spheres were sanded to yield a spherical shape. Sphere diameters of 0.63, 0.95, 1.27, 1.59 and 1.91 cm were used in the tests. The smallest size was limited because of the 0.125 inch diameter cooling manifold; the largest size was limited by the diameter of the flat flame burner.

The porous sphere, with cooling manifold and fuel feed tube attached, was mounted above the flat flame burner. At some minimum height of the sphere above the burner a small,central portion of the flame emitting from the burner was extinguished. As the height above this minimum was increased, the burning rate of the porous sphere increased by as much as 15% for the 1.91 cm sphere. As the height was increased still further, the burning rate decreased.

To account for the variation in burning rate with height above the burner, the highest ambient oxygen concentration condition was used as a baseline. The height of the sphere above the burner was adjusted until the maximum burning rate condition was obtained. This height was used for all testing on a particular size sphere. For the 1.91 cm sphere the height used for testing was 2.5 cm; for the 0.63 cm sphere the height used for testing was 1.5 cm.

Operation of the porous sphere system consisted of setting the burner to give the desired test condition. At the given test condition, the porous sphere was ignited in air; the fuel feed rate was set to give the fully wetted, non-dripping condition. The sphere was then immersed in the burner combustion products and final adjustments were made on the fuel flow rate to yield the stable burning rate.

CHAPTER III

THEORETICAL CONSIDERATIONS

3.1 Existing Theories

Hybrid combustion involves some aspects of both bipropellant and monopropellant combustion. The approach used here for treating the bipropellant flame is fairly standard. Namely, the reaction rate was assumed to be infinitely fast so that kinetic effects could be ignored. However, the treatment of the monopropellant flame requires further explanation.

Monopropellant combustion is inherently more difficult to analyze than bipropellant combustion since kinetic effects must be included in the analysis. The major difference in the existing theories of monopropellant combustion is the way in which kinetic effects are incorporated into the solution. Several theories will be discussed in the following.

Lorell and Wise (14) were among the first investigators to attempt a solution of monopropellant combustion. They assumed that the kinetics could be represented in terms of a single overall reaction rate expression which was suitable for a unimolecular reaction with negligible reverse reaction. The equations developed were solved numerically to find the mass burning rate eigenvalue of the two point boundary value problem defining the problem.

Williams (15) developed a numerical solution by assuming a one step, overall reaction. In addition, he was able to develop an analytical solution for large activation energies, small droplets, and small chemical reaction rates. Williams did allow for the presence of a distributed reaction zone in his analytical solution. However, his method is strictly applicable only to adiabatic burning and the assumption of low reaction rates limits the usefulness of this approach.

Spalding and Jain (16) developed an analytical solution for monopropellant droplet burning rates by using the thin flame approximation. For large activation energies, the temperature dependence of the reaction rate is quite strong. Therefore the bulk of the energy release from the decomposition reaction will occur in a thin shell some distance from the droplet surface under these conditions. Neglecting the effect of curvature on the flame speed, the flame surface was taken to be located at the radial position where the unreacted gas flows into the shell at the laminar burning velocity of the mixture.

By using the thin flame approximation, Spalding (16) was able to derive the droplet burning rate for adiabatic combustion in terms of the laminar flame speed. He assumed the laminar flame speed was a known experimental quantity.

Adler and Spalding (17) presented a solution of the burning rate for premixed flames propagating in the presence of an enthalpy gradient. As a particular example, they discussed the solution for the burning rate of the hybrid combustion case, i.e., the burning of a monopropellant in an oxidizing medium. Using the thin flame approximation and assuming the bipropellant flame radius was much greater than the monopropellant flame radius, Adler and Spalding were able to obtain a solution for the hybrid combustion case.

In a later work by Jain (18), a more detailed analysis of the nonadiabatic burning of monopropellants was presented. Jain again used the thin flame approximation. However, the hybrid combustion case was not considered.

Tarifa (19) assumed the reaction rate was of a particular form in a zone of finite thickness. He developed an approximate analytical solution for the combustion of a monopropellant in an atmosphere of inerts. A global reaction rate of the Arrhenius form was assumed in this analysis.

Fendell (20) also discussed the burning of a monopropellant in an atmosphere of inerts. He presented a closed form analytical solution for the zero activation energy limit.

Dynamic Science Corporation (21) considered the theoretical treatment of hybrid combustion. Their approach was based on that of Tarifa (19). Tarifa's monopropellant theory was extended to include the effects of nonadiabatic burning. However, they assumed that the bipropellant flame radius was much greater than the monopropellant flame radius as did Adler and Spalding (17).

The major difference between the various theories on monopropellant combustion is the manner of treating chemical kinetics. By assuming certain forms for the reaction rate, various investigators (15, 16, 19, 20) developed analytical solutions for adiabatic combustion. Jain (18) developed an analytical solution for the nonadiabatic case. Adler and Spalding (17) and Dynamic Science Corporation (21) treated the hybrid combustion case. However, both assumed the bipropellant flame was effectively an infinite distance from the monopropellant flame.

The present theoretical development did include the effect of a finite bipropellant flame radius. The approach used for treating the monopropellant flame was similar to that of Spalding (16); Spalding's thin flame approximation was used to relate flame position to the laminar burning velocity. The laminar burning velocity was approximated by an Arrhenius type correlation with two adjustable parameters, an activation energy, and a pre-exponential factor.

Spalding's (16) thin flame approach was used instead of one of the other theories for several reasons. Fendell's (20) zero activation energy assumption may or may not be valid for hydrazine type fuel droplet combustion. The assumption certainly does not agree with Eberstein and Glassman's (22) measurements of the chemical kinetics of hydrazine, MMH, and UDMH. The more detailed treatments of Williams (15) and Tarifa (19) could have been used. However, for simplicity Spalding's treatment was preferred.

3.2 General Model

The theoretical model of hybrid combustion consists of a spherical fuel droplet surrounded by a decomposition flame of the fuel gas which is in turn surrounded by an oxidation flame of the decomposition products. The model of the burning droplet is illustrated in Figure 3.

The major assumptions employed in the analysis are as follows:

1. The stagnant film approximation is used for estimating the effect of forced convective flow around the droplet. With this approximation, the gas phase system is

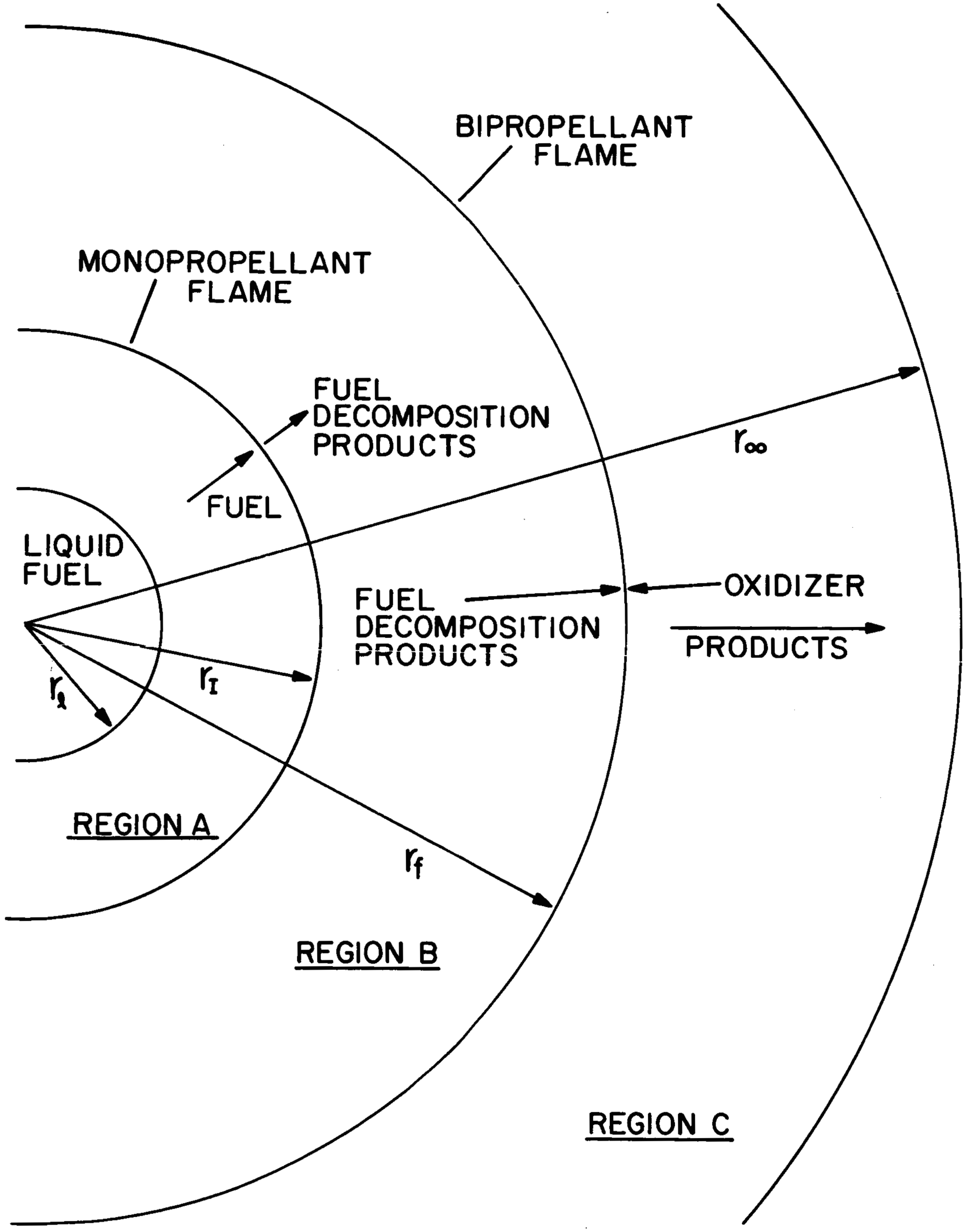

Figure 3 Sketch of the Hybrid Combustion Model

spherically symmetric between the droplet surface and the edge of the stagnant layer, r_∞, as indicated in Figure 3. The approach used to estimate r_∞ will be described later.

2. The droplet is composed of a single chemical species.
3. The total gas pressure is constant throughout Regions A, B, and C of Figure 3. Faeth (23) has shown that this assumption is valid except for droplets much smaller than ones used in the present work.
4. The ideal gas law holds for all species and compressibility effects are neglected. Because of the high temperatures of the gas surrounding the droplet, compressibility effects are small.
5. Thermal diffusion is neglected. Faeth (23) indicated that the mass flux due to thermal diffusion was less than 20% of the concentration diffusion flux for the gas phase surrounding an evaporating iso octane droplet. In addition, treatment of thermal diffusion is extremely complicated. Therefore, inclusion of this phenomena does not appear to be warranted.
6. Radiation effects are neglected. Lazar (24) has shown that radiation contributes only a small fraction of the energy required to vaporize a droplet at moderate pressures.
7. Only steady state conditions are considered. Since the analysis is applied to both droplet and porous sphere

burning, these two cases require further explanation. For the case of a supported droplet, the temperature of the liquid is assumed to be constant and equal to the fuel boiling temperature. The effect of a finite surface regression rate is neglected. These assumptions have been shown (25) to have a negligible effect upon the computed burning rates at moderate pressures. For porous sphere burning, the liquid surface temperature is assumed to equal the fuel boiling temperature. However, the liquid temperature varies within the porous sphere. The energy conducted to the sphere surface supplies the energy required to vaporize the liquid at its boiling temperature plus the energy required to raise the liquid temperature from its supply temperature to the boiling temperature.

8. The monopropellant flame is assumed to be located at the radial position where the unreacted gas flows into the flame surface at the laminar burning velocity of the mixture. This assumption corresponds to Spalding's thin flame approximation (16).
9. The bipropellant reaction is confined to an infinitely thin surface where fuel decomposition products and oxidizer combine in stoichiometric proportion. Brzustowski (26) has shown that this assumption is valid when the product of pressure and droplet diameter exceeds a given limit.

The experimental conditions of the present investigation are above the limit determined by Brzustowski. At the bipropellant flame surface, the concentrations of fuel and oxidizer are taken to be zero.

10. The Lewis number of the oxidizer is assumed to be unity.
11. All specific heats are assumed constant.
12. The thermal conductivity in Regions A, B, and C are assumed to be a linear function of temperature.
13. All gaseous, non-fuel, species are insoluble in the liquid phase.

3.3 Governing Equations

Using the assumptions of the preceding section, the equations of conservation of mass, energy, and species were obtained from the general equations presented by Williams (27) and are applicable for all regions surrounding the droplet. Employing spherical symmetry these equations are:

$$4\pi r^2 \rho v = \dot{M} = \text{constant} \qquad \text{(Mass)} \tag{3.1}$$

$$\frac{d}{dr}\left[\dot{m}\sum_{i=1}^{N} h_i \varepsilon_i - \lambda r^2 \frac{dT}{dr}\right] = 0 \qquad \text{(Energy)} \tag{3.2}$$

$$r^2 \rho D \frac{dY_i}{dr} + \dot{m}(\varepsilon_i - Y_i) = 0 \qquad \text{(Species)} \tag{3.3}$$

where

$$\dot{m} = \frac{\dot{M}}{4\pi} \tag{3,4}$$

and the mass flux fraction of species i, ε_i, is defined by the equation

$$\rho v \varepsilon_i = \rho Y_i (v + U_i) \tag{3.5}$$

Since all gaseous species are insoluble in the liquid phase except the fuel and both the monopropellant and bipropellant flames are restricted to infinitely thin surfaces, only certain diffusing species are present in each of the Regions A, B, and C. In Region A only fuel is diffusing. In Region B only fuel decomposition products are diffusing. In Region C only oxidizer and oxidation flame products are diffusing. Therefore $\varepsilon_{FP} = 1$ in Region B and $\varepsilon_F = 1$ in Region A.

In Region C the values of ε_P and ε_o are related to the stoichiometric coefficient, γ, which is defined by the equation

$$\gamma = \frac{-\dot{m}_o}{\dot{m}_{FP}} \tag{3.6}$$

Since the mass flow rate of fuel decomposition products into the bipropellant flame must equal the total mass flow rate, $\dot{m}$, in Region B, ε_o, ε_P, and γ are related by the equations

$$\varepsilon_o = \gamma \tag{3.7}$$

$$\varepsilon_P = 1 + \gamma \tag{3.8}$$

in Region C.

Using the above results and integrating Equation (3.2) in Region A yields:

$$\dot{m}\, h_F - \lambda_A\, r^2 \frac{dT}{dr} = \left[\dot{m}\, h_F - \lambda_A\, r^2 \frac{dT}{dr}\right]_{r_\ell^+} \tag{3.9}$$

The right-hand side of Equation (3.9) can be evaluated by applying conservation of energy at the droplet surface. Under the steady burning assumption all the energy reaching the droplet surface goes into the heat of vaporization of the liquid fuel. This is expressed as:

$$\dot{m}\, L = \lambda_A\, r^2 \frac{dT}{dr}\Big]_{r_\ell^+} \tag{3.10}$$

where L must also include any liquid phase enthalpy rise of the fuel for the porous sphere case. Introducing Equation (3.10) into Equation (3.9) results in:

$$\dot{m}(h_F - h_{F,\ell} + L) = \lambda_A\, r^2 \frac{dT}{dr} \tag{3.11}$$

Equation (3.2) integrated in Region B becomes:

$$\dot{m}\, h_{FP} - \lambda_B\, r^2 \frac{dT}{dr} = \left[\dot{m}\, h_{FP} - \lambda_B\, r^2 \frac{dT}{dr}\right]_{r_I^+} \tag{3.12}$$

The right-hand side of Equation (3.12) can be evaluated by considering the conservation of energy across the flame at $r = r_I$, i.e.,

$$\left[\dot{m}\, h_F - \lambda_A\, r^2 \frac{dT}{dr}\right]_{r_I^-} = \left[\dot{m}\, h_{FP} - \lambda_B\, r^2 \frac{dT}{dr}\right]_{r_I^+} \tag{3.13}$$

Noting the boundary condition of Equation (3.9), (3.13) becomes

$$\left[\dot{m}\,h_F - \lambda_A\,r^2\,\frac{dT}{dr}\right]_{r_I^-} = \dot{m}(h_{F,\ell} - L) \tag{3.14}$$

Introducing Equations (3.13) and (3.14) into (3.12) yields:

$$\dot{m}(h_{FP} - h_{F,\ell} + L) = \lambda_B\,r^2\,\frac{dT}{dr} \tag{3.15}$$

Integrating Equation (3.2) in Region C results in the following:

$$\dot{m}\left[(1+\gamma)h_P - \gamma h_o\right] - \lambda_C\,r^2\,\frac{dT}{dr} = \left\{\dot{m}\left[(1+\gamma)h_P - \gamma h_o\right] - \lambda_C\,r^2\,\frac{dT}{dr}\right\}_{r_f^+} \tag{3.16}$$

Following the same procedure as before, the conservation of energy is applied across the flame at $r = r_f$. However, the energy is constant in Region B and equal to the total energy in Region A. The final result for Region C:

$$\dot{m}[(1+\gamma)h_P - \gamma h_o - h_{F,\ell} + L] = \lambda_C\,r^2\,\frac{dT}{dr} \tag{3.17}$$

The enthalpy of any species i is related to its heat of formation at a standard temperature, T°, through the equation:

$$h_i = h_i - h_i^\circ + \Delta H_i^\circ \tag{3.18}$$

The equations obtained by substituting Equation (3.18) into the energy equations for Regions A, B, and C are simplified by defining two new variables as follows:

$$q_1 \equiv \Delta H^\circ_{FP} - \Delta H^\circ_F + L - (h_{F,\ell} - h^\circ_F) \qquad (3.19)$$

$$q_2 \equiv (1+\gamma)\ \Delta H^\circ_P - \gamma \Delta H^\circ_o - \Delta H^\circ_F + L - (h_{F,\ell} - h^\circ_F) \qquad (3.20)$$

Using the assumption of constant specific heats and substituting Equations (3.18)-(3.20) into Equations (3.11), (3.15), and (3.17) yields the following set of equations:

$$\dot{m}[C_F(T-T^\circ) + L] = \lambda_A\ r^2 \frac{dT}{dr} \qquad \text{(Region A)} \qquad (3.21)$$

$$\dot{m}[C_{FP}(T-T^\circ) + q_1] = \lambda_B\ r^2 \frac{dT}{dr} \qquad \text{(Region B)} \qquad (3.22)$$

$$\dot{m}[\sigma(T-T^\circ) + q_2] = \lambda_C\ r^2 \frac{dT}{dr} \qquad \text{(Region C)} \qquad (3.23)$$

where

$$\sigma \equiv (1+\gamma)C_P - \gamma C_o \qquad (3.24)$$

The boundary conditions applicable to Equations (3.21), (3.22) and (3.23) are as follows:

for Equation (3.21)

$$r = r_\ell \quad T = T_\ell\ ; \quad r = r_I \quad T = T_I \qquad (3.25)$$

for Equation (3.22)

$$r = r_I \quad T = T_I\ ; \quad r = r_f \quad T = T_f \qquad (3.26)$$

and for Equation (3.23)

$$r = r_f \quad T = T_f \; ; \quad r = r_\infty \quad T = T_\infty \tag{3.27}$$

where r_ℓ, T_ℓ, r_∞, and T_∞ are known quantities.

Introducing the assumption that the thermal conductivities vary linearly with temperature in each region, i.e.,

$$\lambda_j = \lambda_{j\ell}(T/T_\ell) \tag{3.28}$$

and using the appropriate boundary conditions, Equations (3.21), (3.22), and (3.23) can be integrated. The resulting equations are simplified by introducing dimensionless variables as follows:

$$\beta = \frac{r}{r_\ell} \tag{3.29}$$

$$\theta = \frac{T}{T_\infty} \tag{3.30}$$

$$L^* = \frac{L}{C_F T_\infty} \tag{3.31}$$

$$Q_1 = \frac{q_1}{C_{FP} T_\infty} \tag{3.32}$$

$$Q_2 = \frac{q_2}{\sigma T_\infty} \tag{3.33}$$

The integrated equations are:

$$\frac{\dot{m}\, C_F}{\lambda_{A\ell} r_\ell} \left(1 - \frac{1}{\beta_I}\right) = \frac{1}{\theta_\ell} \left[\theta_I - \theta_\ell - \left(L^* - \theta_\ell\right) \ln \frac{\theta_I - \theta_\ell + L^*}{L^*}\right] \tag{3.34}$$

$$\frac{\dot{m}\, C_{FP}}{\lambda_{B\ell} r_{\ell}}\left(\frac{1}{\beta_I} - \frac{1}{\beta_f}\right) = \frac{1}{\theta_{\ell}}\left[\theta_f - \theta_I - \left(Q_1 - \theta^\circ\right)\ln\frac{\theta_f - \theta^\circ + Q_1}{\theta_I - \theta^\circ + Q_1}\right] \quad (3.35)$$

$$\frac{\dot{m}\, \sigma}{\lambda_{C\ell} r_{\ell}}\left(\frac{1}{\beta_f} - \frac{1}{\beta_\infty}\right) = \frac{1}{\theta_{\ell}}\left[1 - \theta_f - \left(Q_2 - \theta^\circ\right)\ln\frac{1 - \theta^\circ + Q_2}{\theta_f - \theta^\circ + Q_2}\right] \quad (3.36)$$

An additional equation can be generated without introducing additional unknowns by considering the conservation of species applied to the oxidizer in Region C. Equation (3.3) applied to the oxidizer in Region C becomes:

$$\frac{\lambda_C}{C_0 Le_0}\, r^2 \frac{dY_0}{dr} = \dot{m}(\gamma + Y_0) \quad (3.37)$$

where $Le_0 \equiv \frac{\lambda_C}{C_0(\rho D)_0}$ is the Lewis number for the oxidizer (assumed to equal unity). Dividing Equation (3.23) by Equation (3.37) results in:

$$\frac{\sigma(T - T^\circ) + q_2}{\gamma + Y_0} = C_0 \frac{dT}{dY_0} \quad (3.38)$$

The appropriate boundary conditions for Equation (3.38) are as follows:

$$T = T_f \quad Y_0 = 0 \;\; ; \;\; T = T_\infty \quad Y_0 = Y_{0\infty} \quad (3.39)$$

The concentration of the oxidizer far from the droplet, $Y_{0\infty}$, is assumed to be a known quantity. Integrating Equation (3.38) with boundary conditions, Equation (3.39), and introducing Equation (3.30) and (3.33) yields:

$$\theta_f = (1 - \theta^\circ + Q_2)/\left(\frac{\gamma+Y_{0\infty}}{\gamma}\right)^{\sigma/C_0} + \theta^\circ - Q_2 \qquad (3.40)$$

Equations (3.34), (3.35), (3.36), and (3.40) comprise a set of four equations in five unknowns, β_I, β_f, θ_I, θ_f, and $\dot{m}$. The additional equation required is generated through the use of a laminar flame velocity expression.

Comparing Equations (3.4) and (3.1) it is clear that

$$\dot{m} = r^2 \rho v = \text{constant} \qquad (3.41)$$

and therefore

$$\dot{m} = r_I^{\ 2}(\rho v)_I \qquad (3.42)$$

Assuming that $(\rho v)_I$ can be represented in terms of a laminar flame velocity expression, i.e.,

$$(\rho v)_I = A \exp\left(\frac{-E}{2RT_I}\right) \qquad (3.43)$$

then

$$\dot{m} = \beta_I^{\ 2}\, r_\ell^{\ 2}\, A \exp\left(\frac{-E}{2R\theta_I T_\infty}\right) \qquad (3.44)$$

constitutes the additional required equation. A represents a pre-exponential factor which may also carry any pressure dependence of the laminar flame expression; E is an activation energy. Both A and E are assumed to be a constant for each fuel at a given total pressure.

The five equations, Equations (3.34), (3.35), (3.36), (3.40) and (3.44) form a closed set for the five unknowns, β_I, β_f, θ_I, θ_f and $\dot{m}$ for the hybrid combustion case. This set of equations can be simplified for several limiting cases. These limiting cases, pure monopropellant combustion, pure bipropellant combustion, and pure evaporation, are discussed in the following.

For pure monopropellant combustion, the concentration of oxidizer in the ambient surroundings is zero. From Equation (3.40)

$$\theta_f = 1 \tag{3.45}$$

and from Equation (3.36)

$$\beta_f = \beta_\infty \tag{3.46}$$

Thus, the equations applicable to pure monopropellant combustion are:

$$\frac{\dot{m}\ C_F}{\lambda_{A\ell} r_\ell}\left(1 - \frac{1}{\beta_I}\right) = \frac{1}{\theta_\ell}\left[\theta_I - \theta_\ell - (L^* - \theta_\ell)\ \ln\ \frac{\theta_I - \theta_\ell + L^*}{L^*}\right] \tag{3.47}$$

$$\frac{\dot{m}\ C_{FP}}{\lambda_{B\ell} r_\ell}\left(\frac{1}{\beta_I} - \frac{1}{\beta_\infty}\right) = \frac{1}{\theta_\ell}\left[1 - \theta_I - (Q_1 - \theta^\circ)\ \ln\ \frac{1 - \theta^\circ + Q_1}{\theta_I - \theta^\circ + Q_1}\right] \tag{3.48}$$

$$\dot{m} = \beta_I^{\,2}\ r_\ell^{\,2}\ A\ \exp\left(\frac{-E}{2R\theta_I T_\infty}\right) \tag{3.49}$$

These three equations, Equations (3.47), (3.48), and (3.49), form a closed set for the three unknowns, β_I, θ_I, and $\dot{m}$.

As Region B in Figure 3 becomes increasingly narrower, β_I approaches β_f. At the point where β_I equals β_f, the situation corresponds to pure bipropellant combustion and the hybrid combustion characteristic is lost. From Equation (3.35), θ_I must equal θ_f for β_I equal to β_f. Thus the equations for pure bipropellant combustion reduce to:

$$\frac{\dot{m}\, C_F}{\lambda_{A\ell} r_\ell}\left(1 - \frac{1}{\beta_f}\right) = \frac{1}{\theta_\ell}\left[\theta_f - \theta_\ell - (L^* - \theta_\ell)\ \ln \frac{\theta_f - \theta_\ell + L^*}{L^*}\right] \tag{3.50}$$

$$\frac{\dot{m}\, \sigma}{\lambda_{C\ell} r_\ell}\left(\frac{1}{\beta_f} - \frac{1}{\beta_\infty}\right) = \frac{1}{\theta_\ell}\left[1 - \theta_f - (Q_2 - \theta^\circ)\ln \frac{1 - \theta^\circ + Q_2}{\theta_f - \theta^\circ + Q_2}\right] \tag{3.51}$$

$$\theta_f = (1 - \theta^\circ + Q_2)/\left(\frac{\gamma + Y_{O\infty}}{\gamma}\right)^{\sigma/C_O} + \theta^\circ - Q_2 \tag{3.52}$$

The unknowns for this case are β_f, θ_f, and $\dot{m}$. An equation such as Equation (3.44) is not required since Equations (3.50)-(3.52) form a closet set for the three unknowns.

For evaporation with no combustion, the ambient oxygen concentration is zero and from Equation (3.52), θ_f must equal one. From Equation (3.51) for θ_f equal one β_f must equal β_∞. The equations for pure evaporation reduce to the following:

$$\frac{\dot{m}\,C_F}{\lambda_{A\ell}r_\ell}\left(1-\frac{1}{\beta_\infty}\right)=\frac{1}{\theta_\ell}\left[1-\theta_\ell-(L^*-\theta_\ell)\ln\frac{1-\theta_\ell+L^*}{L^*}\right] \tag{3.53}$$

The solution for the hybrid and pure monopropellant combustion cases involves the parameters A and E in the laminar flame velocity expression. These parameters are not experimentally known for droplet combustion for the fuels of interest. Thus the parameters A and E had to be estimated from the experimental data. The procedure used to compute these parameters is explained in the following.

In order to compute the empirical parameters, A and E, an experimental $\dot{m}$ for some mid-range test condition was selected. Then, picking a value for E, A was computed so that the experimental $\dot{m}$ and computed $\dot{m}$ were matched. Using these same values for A and E, the mass burning rate, $\dot{m}$, was computed for other test conditions. In this manner a set of computed mass burning rates was obtained for each value of E for comparison with the remainder of the data.

The approach used to estimate the value of the dimensionless infinite radius, β_∞, will now be explained. For zero convection conditions, β_∞ equals infinity. However, the experiments were conducted under forced convection conditions. To estimate the effect of forced convective flow around the drop, a film theory as discussed by Faeth (28) was employed. With this approximation for convection effects the outer film dimensionless radius, β_∞, is given at any flow condition by the following:

$$\beta_\infty = \frac{Nu}{Nu-2} \tag{3.54}$$

where Nu is the Nusslet number in the absence of mass transfer and chemical reaction.

The Nusselt number for any flow condition was estimated using the correlation developed by Lazar [24]. The correlation is as follows:

$$\frac{Nu}{Nu^*} = 1 + 0.278\, Re^{1/2}\, Pr^{1/3} \left[1 + 1.237\, Re^{-1}\, Pr^{-4/3}\right]^{-1/2} \tag{3.55}$$

where Nu* is the Nusslet number for the no flow condition. As suggested by Combs (29), properties in the correlation were taken to be those of the ambient gases since this method eliminates the difficulties in defining unambiguous mean properties. The correlations used for the ambient gas properties required for the estimation of the Reynolds and Prandtl numbers are given in Appendix A.

Experimental mass burning rates, $\dot{M}$, are compared with predicted values using the theoretical model in the next chapter. The properties used in the model are listed in Table 2. The specific correlations and references used to determine these properties are given in Appendix A.

Table 2

Properties Used in the Theoretical Models

Property	Fuel		
	N_2H_4	MMH	UDMH
T_ℓ (K)	387	361	336
γ	1.00	1.74	2.13
L (cal/gm)	334	209	139
q_1 (cal/gm)	-748	-708	-334
q_2 (cal/gm)	-4630	-6180	-7220
C_F (cal/gm-K)	0.696	0.751	0.807
C_{FP} (cal/gm-K)	0.800	0.854	0.871
C_P (cal/gm-K)	0.540	0.500	0.481
C_O (cal/gm-K)	0.290	0.290	0.290
$\lambda_{A\ell} \times 10^4$ (cal/cm-sec-K)	1.0	1.1	0.77
$\lambda_{B\ell} \times 10^4$ (cal/cm-sec-K)	1.2	1.2	0.90
$\lambda_{C\ell} \times 10^4$ (cal/cm-sec-K)	0.83	0.73	0.65

CHAPTER IV

RESULTS AND DISCUSSION

4.1 Data Reduction

The high temperature droplet burning rate data was obtained using two somewhat different experimental techniques. The small diameter burning rates were obtained from the diameter variation with time of a suspended droplet. Data for the larger diameters was obtained directly from the mass rate of fuel supplied internally to a burning porous sphere. The method of data reduction for the suspended droplet tests and the applicability of comparing the data obtained in these two different ways are discussed in the following.

The suspended droplet experiments yielded the time variation of droplet diameter. When this data was plotted as diameter squared as a function of time, reasonably linear curves were obtained. A sample diameter squared plot for three tests with UDMH is shown in Figure 4. Burning rate constants were obtained by measuring the slope of these curves. The slopes were determined by fitting a least squares curve to the data for each test. Since droplet burning rates vary with droplet diameter, the slopes were balanced about a fixed average diameter (on the order of 1200μ).

For each test condition, the measured burning rate constants were an average of three separate tests. A statistical analysis of the data indicated that the percent standard deviation of the slopes

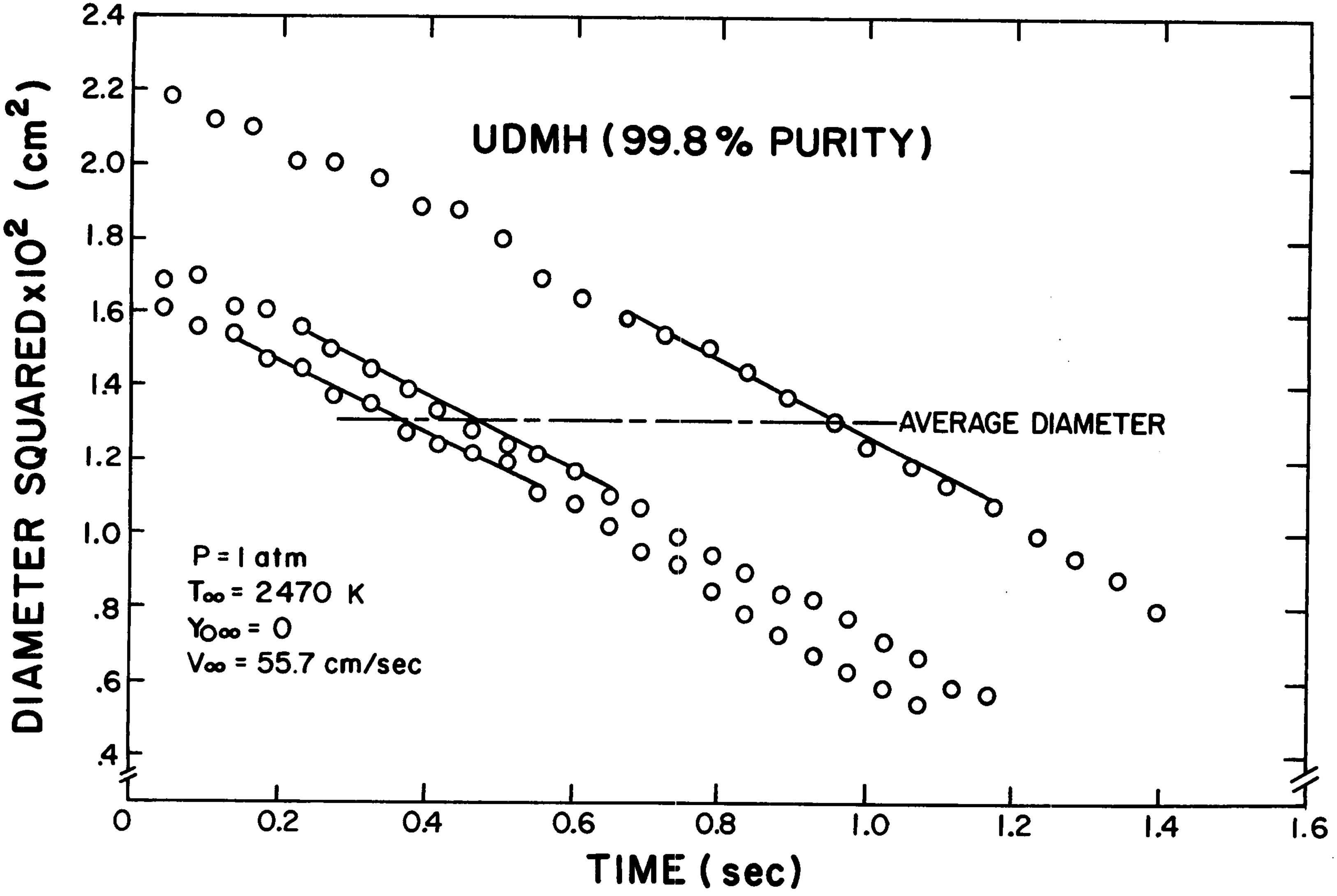

Figure 4 Typical Diameter Squared Plots Used to Determine Burning Rates

obtained from the least squares curves did not exceed 5% for any reported test.

The effect of the diameter of the quartz support fiber on the results for the suspended droplet tests was investigated during preliminary testing. It was found that doubling the diameter of the fiber from 100 to 200μ resulted in a 15% increase in the burning rate constant. This suggests that the present results (100μ fiber) may be somewhat in excess of the burning rate constants of free droplets.

For comparison with the porous sphere data, burning rate constants had to be converted to mass burning rates. The relationship between the burning rate constant, K, and the mass burning rate, $\dot{M}$, as given by Williams (27) is:

$$\dot{M} = K \pi \rho_{\ell} r_{\ell}/2 \tag{4.1}$$

Experimental burning rate constants and computed mass burning rates from Equation (4.1) are listed in Appendix B for all test conditions and the three fuels tested.

Mass burning rates were obtained directly with the porous sphere experimental technique. The porous sphere data is also listed in Appendix B. Spot checks for various test conditions from day to day indicated that mass burning rates could be reproduced within about ±3% with this technique.

The total heat of vaporization, L, differed in numerical value for the two experimental techniques. In the case of a porous sphere, L included the energy required for sensible heating of the liquid from its entering temperature (298 K) to the fuel boiling temperature. However, the theoretical difference in mass burning rate for the different L values did not exceed 3% for any test condition. Therefore, the mass burning rates for the two experimental techniques are, for all practical purposes the same for a given drop diameter and test condition.

Figure 5 shows photographs of burning porous spheres under various conditions. For oxidation conditions all fuels exhibited a flame with two distinct zones of luminosity. This phenomena is characteristic of hybrid combustion of the hydrazine fuels. Lawver, et al., (8) observed similar behavior for hydrazine burning in nitrogen tetroxide. However, Lawver also indicated that the visible flame fronts did not coincide with the maximum temperature points in the flame for their test conditions. Therefore the visible fronts may or may not indicate the position of the monopropellant and bipropellant flames. The hydrazine flame is seen to be somewhat more spherical than that for UDMH in Figure 5. MMH burning under oxidation conditions was similar in appearance to UDMH.

For decomposition conditions, no visible flame front could be seen for any of the three fuels. Hydrazine and MMH burning under decomposition conditions are also shown in Figure 5.

Figure 5 also illustrates the presence of small drops on the bottom side of the porous sphere. These small drops were used as an indication of the steady burning condition. At the steady burning condition this small drop did not grow or diminish in size. A stable burning condition could not be obtained if the drop

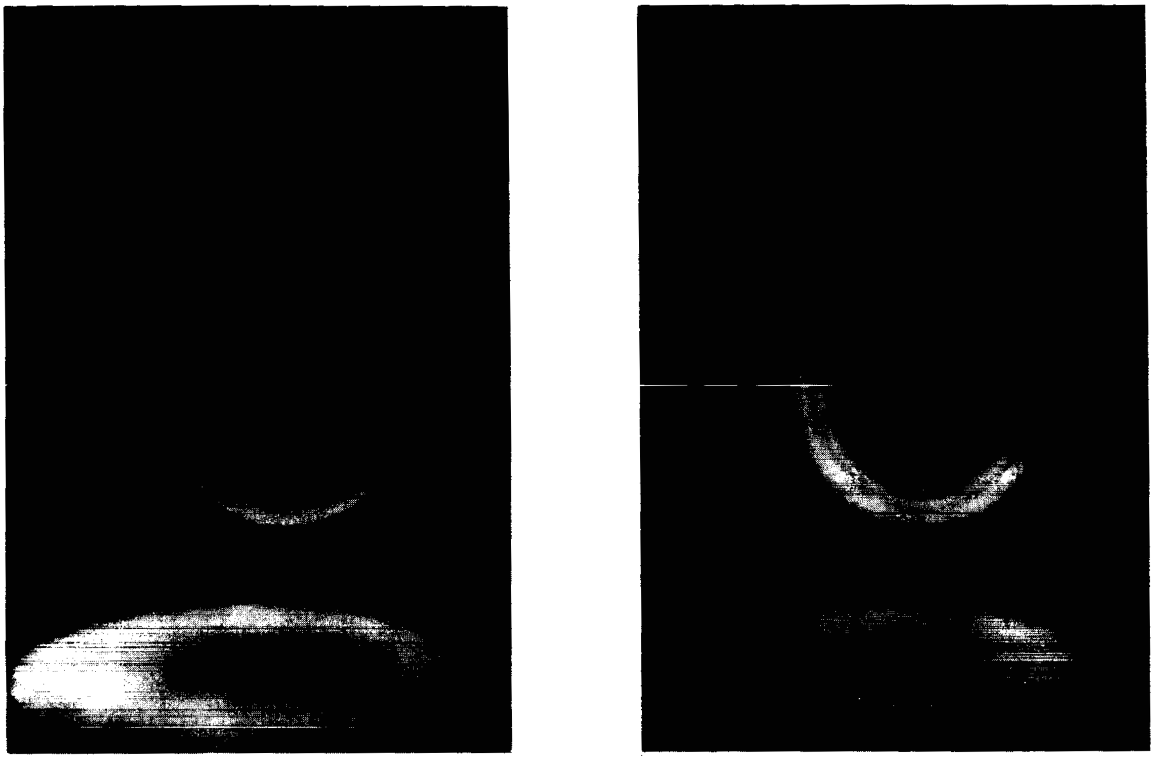

N_2H_4, $d_\ell=1.27\text{cm}$, $T_\infty=2530\text{K}$, $Y_{O\infty}=0.418$ UDMH, $d_\ell=1.27\text{cm}$, $T_\infty=2530\text{K}$, $Y_{O\infty}=0.418$

N_2H_4, $d_\ell=1.27\text{cm}$, $T_\infty=1835\text{K}$, $Y_{O\infty}=0$ MMH, $d_\ell=1.27\text{cm}$, $T_\infty=1835\text{K}$, $Y_{O\infty}=0$

Figure 5 Photographs of Burning Porous Spheres for Various Test Conditions did not appear; for with no drop present, the porous sphere became dry and overheated.

Some indication of the effect of the small drop on the burning rate of the porous sphere can be obtained by comparing the surface area of the porous sphere to the surface area of the porous sphere with the small drop attached. The increase in surface area, for the worst condition shown in Figure 5, is less than 3%.

Since the hybrid combustion model required numerical values for the parameters A and E, these parameters were estimated from the data. Table 3 shows the values of A and E used in the hybrid model for all three fuels. Also shown on Table 3 are the correlation conditions used to compute A with the given value of E and $\dot{M}$.

For zero activation energy, A corresponds to the mass burning rate per unit area of a plane laminar flame. Antoine (30) reported values of laminar flame speed for hydrazine taken from measurements reported using the strand burning technique. At atmospheric pressure Antoine's reported value of the laminar flame speed corresponds to a mass burning rate per unit area of 0.019 gm/cm^2-sec. The present computed value of A (with E=0) for hydrazine is 0.0136 gm/cm^2-sec. Thus, the present results seem to be compatible with strand burning measurements at least for the one condition where the two can be compared. No measurements of the laminar flame speed of MMH or UDMH could be found in the literature.

As discussed in the theory chapter, the effect of forced convective flow past the burning droplet was accounted for by assuming a stagnant film of dimensionless radius β_∞. Table 4 lists

Table 3

Correlation Conditions and Parameters Used in the Hybrid Model

Fuel	Correlation Condition				A	E
	T_∞(K)	$Y_{O\infty}$	d_ℓ(cm)	$\dot{M}$(gm/sec)	(gm/cm^2-sec)	(kcal/mole)
N_2H_4	2470	0	0.95	0.0420	0.0136	0
					0.1040	10
					6.106	30
MMH	2470	0	1.27	0.0205	0.0025	0
					0.0116	10
					0.2486	30
UDMH	2470	0	1.27	0.0218	0.0038	0
					0.1033	10
					77.88	30

Table 4

Convection Correction for Hydrazine for Various Test Conditions

$Y_{O\infty}$	T_∞ (K)	d_ℓ (cm)	Re	Pr	β_∞	$\dot{M}/\dot{M}^*$	
						Bipropellant	Hybrid
0.043	2530	0.13	1.529	0.683	6.066	1.195	1.086
0.043	2530	0.95	11.47	0.683	2.310	1.762	1.000
0.043	2530	1.91	22.94	0.683	1.890	2.120	1.000
0.233	2530	0.13	1.503	0.687	6.104	1.198	1.135
0.233	2530	0.95	11.27	0.687	2.319	1.756	1.008
0.233	2530	1.91	22.55	0.687	1.896	2.115	1.000
0.418	2530	0.13	1.480	0.690	6.152	1.196	1.158
0.418	2530	0.95	11.10	0.690	2.323	1.753	1.045
0.418	2530	1.91	22.19	0.690	1.903	2.105	1.000
0	2330	0.13	1.971	0.683	5.157	1.239	1.050
0	2330	0.95	14.79	0.683	2.133	1.886	1.000
0	2330	1.91	29.57	0.683	1.777	2.290	1.000
0	2060	0.13	2.159	0.688	4.864	1.261	1.035
0	2060	0.95	16.19	0.688	2.074	1.930	1.000
0	2060	1.91	32.38	0.688	1.738	2.357	1.000
0	1835	0.13	2.342	0.694	4.621	1.276	1.028
0	1835	0.95	17.57	0.694	2.024	1.975	1.000
0	1835	1.91	35.14	0.694	1.705	2.415	1.000
0	1660	0.13	2.515	0.700	4.420	1.292	1.020
0	1660	0.95	18.87	0.700	1.981	2.015	1.000
0	1660	1.91	37.73	0.700	1.677	2.490	1.000

values of β_∞, Reynolds number, and Prandtl number for various test conditions. The correlations used to estimate the Reynolds and Prandtl numbers are given in Appendix A. Also listed in Table 4 is the ratio of mass burning rate computed for convective flow to the mass burning rate for no flow conditions for hydrazine for both the bipropellant and hybrid models.

As indicated in Table 4, as droplet diameter increased at a given test condition the effect of forced convection (based on the values of $\dot{M}/\dot{M}^*$) increased the mass burning rate for the bipropellant model as much as 2.5 times over the mass burning rate for no flow conditions for the largest sphere size tested. However, the hybrid model was quite insensitive to ambient conditions. In fact, as drop diameter increased the effect of convective flow decreased. This phenomena will be discussed in greater detail later.

As noted in the Introduction four fuels were to be tested, namely, hydrazine, MMH, UDMH, and A-50. No experimental data was taken for A-50 although attempts were made to obtain data using both the suspended droplet and porous sphere techniques. In the case of a suspended droplet, the liquid A-50 formed bubbles and shattered before sufficient time had elapsed to obtain a diameter history of the droplet. For porous sphere burning the liquid burst from the surface of the sphere in the form of small droplets; a stable burning condition could not be obtained even for combustion in air at room temperature. Lawver, et al., (8) noted similar behavior for mixtures of hydrazine and UDMH containing more than 5% UDMH by weight.
No attempt was made to determine the cause of this erratic behavior for A-50.

Also investigated during the experimental program was the effect of water vapor in the ambient gas on the burning rate. Within experimental error, it was found that ambient water vapor mass fractions as high as 0.14 had no effect on the burning rates at a given temperature, ambient oxygen concentration, and drop diameter.

The experimental data is compared to the predicted data using the various models in the following sections.

4.2 Effect of Drop Diameter

The droplet sizes normally found in spray combustion phenomena are at least an order of magnitude smaller than the smallest drop sizes considered in this experimental program. Therefore, the data must be extrapolated over a large range in order to predict burning rates for drop sizes found in spray combustion. For this reason the effect of droplet diameter on mass burning rates is an important experimental consideration.

Figure 6 is a typical plot of the mass burning rate of hydrazine as a function of drop diameter for an oxidation condition. Also shown are the predicted mass burning rates using the hybrid model with various activation energies and the bipropellant model.

The bipropellant results are shown as bands rather than single curves in Figure 6. A parametric study indicated that bipropellant mass burning rates were most sensitive to a change in the thermal conductivity in the region adjacent to the droplet surface (Region A of Figure 3). The bands shown in Figure 6 give the limits resulting from a ±20% variation on $\lambda_{A\ell}$. Since the hybrid model requires a

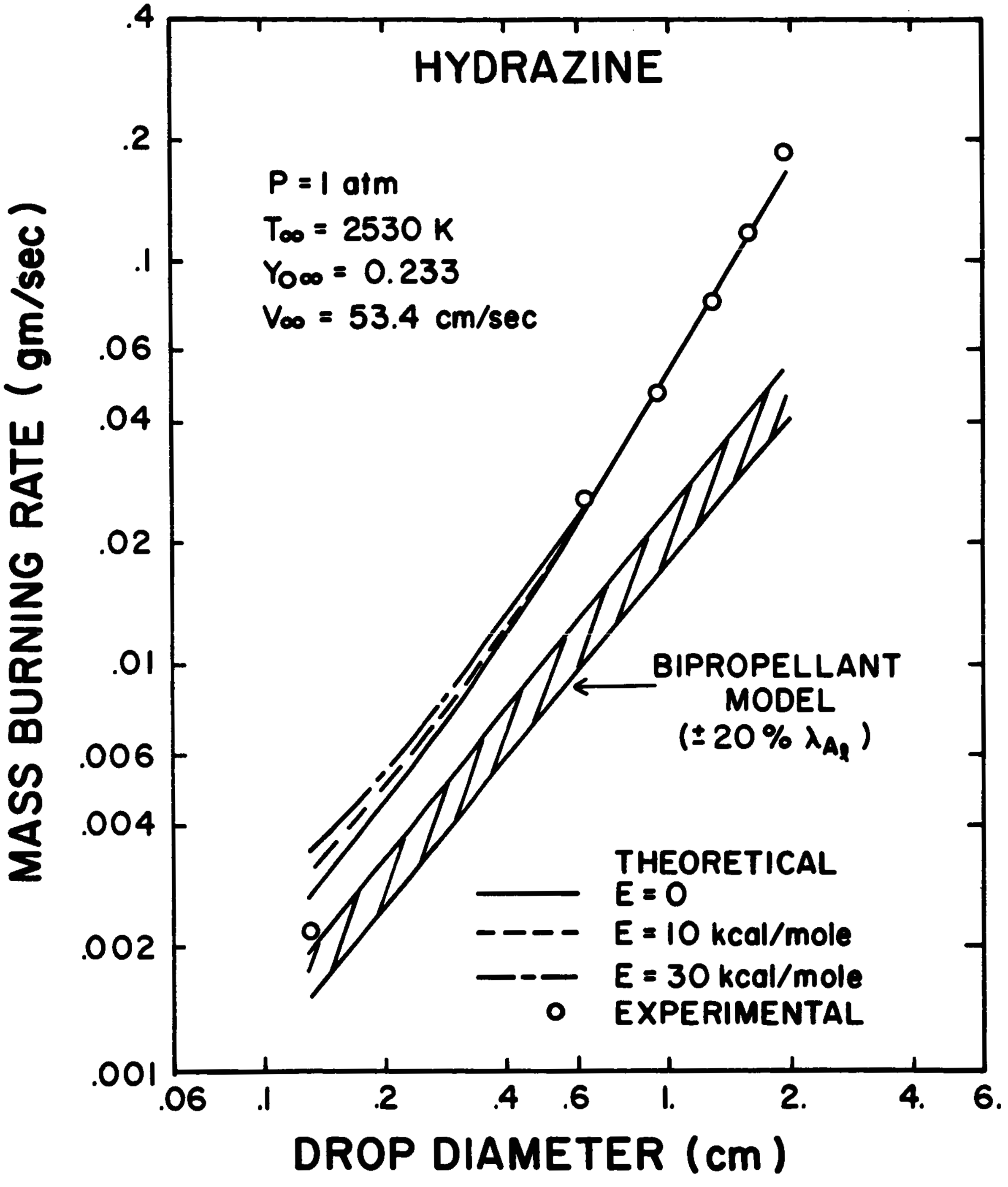

Figure 6 Hydrazine Burning Rates at a Typical Oxidation Condition for Various Drop Diameters

calculation of A for each fuel, a variation in $\lambda_{A\ell}$ is merely absorbed in the calculated A.

As indicated on Figure 6, the bipropellant model predicts the mass burning rate of the small droplet fairly well. However, as droplet diameter increases the data deviates considerably from the bipropellant solution. For the largest diameter drop, the bipropellant solution is almost 4 times lower than the experimental value.

The hybrid model does predict the tread of $\dot{M}$ with diameter in Figure 6. Also, one can note that the solutions for various activation energies asymptotically approach one another for large diameters. For the conditions of Figure 6 the temperature independent laminar flame velocity expression (E=0) gives the best prediction of the experimental data.

Figure 7 is a similar plot for hydrazine except that a decomposition condition is shown. In this case, the evaporation model predicts mass burning rates which are low by almost an order of magnitude for the largest diameter sphere. Again, the hybrid model does predict the data with a temperature independent laminar flame velocity expression giving the best overall prediction.

By comparing the results in Table 4 with the trends indicated in Figures 6 and 7, one can obtain a plausible explanation as to why the effect of convective flow decreases with increasing drop diameter for hydrazine and for the hybrid model. For small diameters the hybrid solution approaches the bipropellant solution while for large diameters the hybrid solution deviates significantly indicating the onset of monopropellant like behavior. Since for large diameters

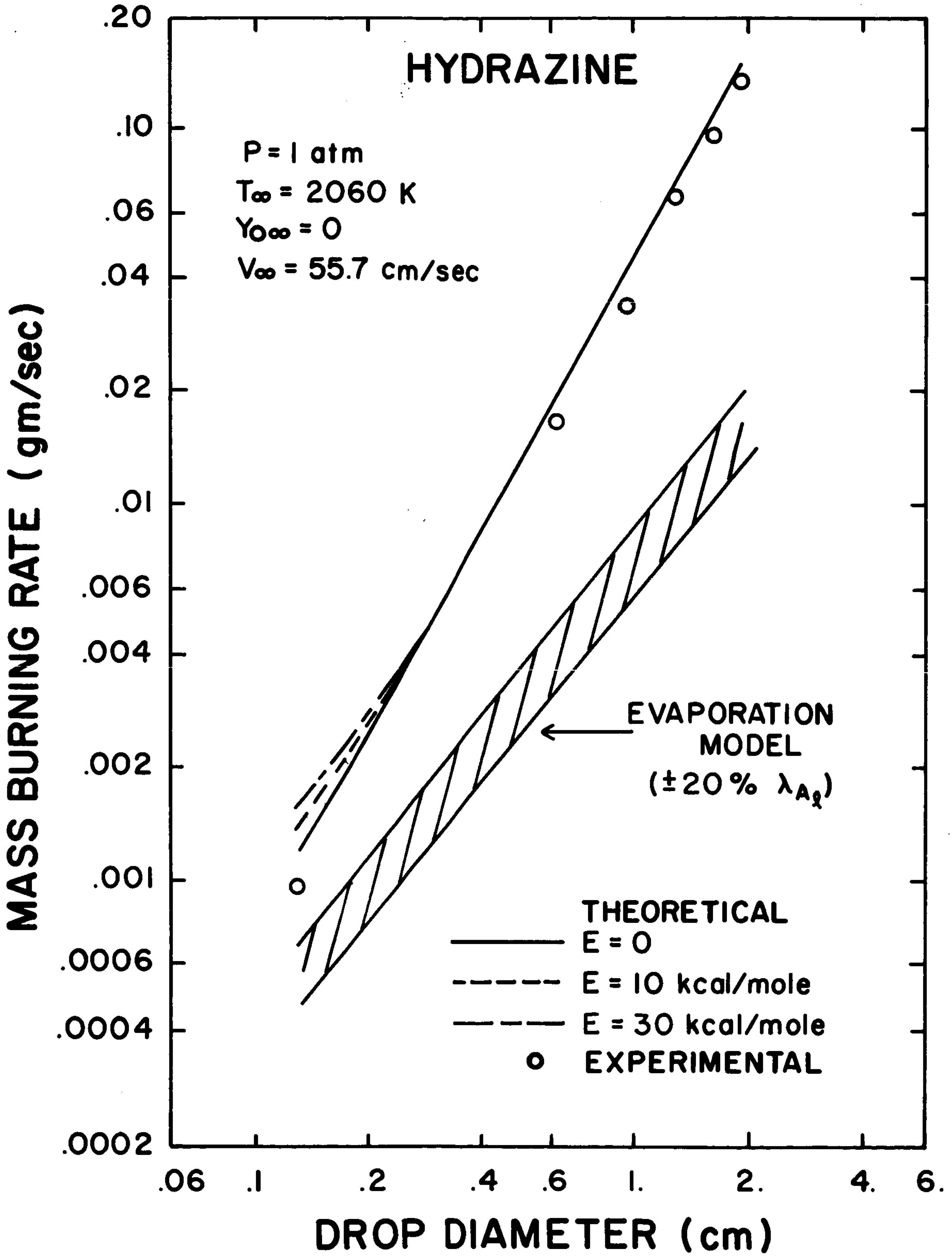

Figure 7 Hydrazine Burning Rates at a Typical Decomposition Condition for Various Drop Diameters

convective flow has no effect on the computed hybrid mass burning rate, monopropellant like behavior is highly insensitive to ambient conditions.

Figures 8 and 9 are typical plots of $\dot{M}$ as a function of drop diameter for MMH for an oxidation and a decomposition condition respectively. Bands of $\pm 20\%$ $\lambda_{A\ell}$ are not shown in order to avoid cluttering the figure, however, these ranges are similar to those shown on Figures 6 and 7. As indicated on Figure 8 the bipropellant model does predict experimental mass burning rates of MMH fairly well over the entire range of drop sizes considered. At small diameters, the hybrid solution for E=0 and the bipropellant solution merge together. Theoretically this indicates that MMH has lost its monopropellant characteristics. At larger diameters the solutions separate indicating the onset of monopropellant like behavior.

Similar behavior can be noted in Figure 9. In this case, however, the deviation from an evaporation solution is as much as a factor of 2 for large diameters. Here again the hybrid model does predict the trend in the data with a zero activation energy solution superior to a temperature dependent laminar flame velocity solution.

Figures 10 and 11 are similar plots for UDMH. Again the $\pm 20\%$ band of $\lambda_{A\ell}$ for the bipropellant solution is not shown for clarity. Some testing was conducted with high purity UDMH; these results are also indicated in Figures 10 and 11.

UDMH exhibited similar behavior to that of MMH. As shown in Figure 10, the data deviates slightly from a pure bipropellant solution for large diameter. For the decomposition condition of Figure 11 the deviation at large diameters is much more pronounced.

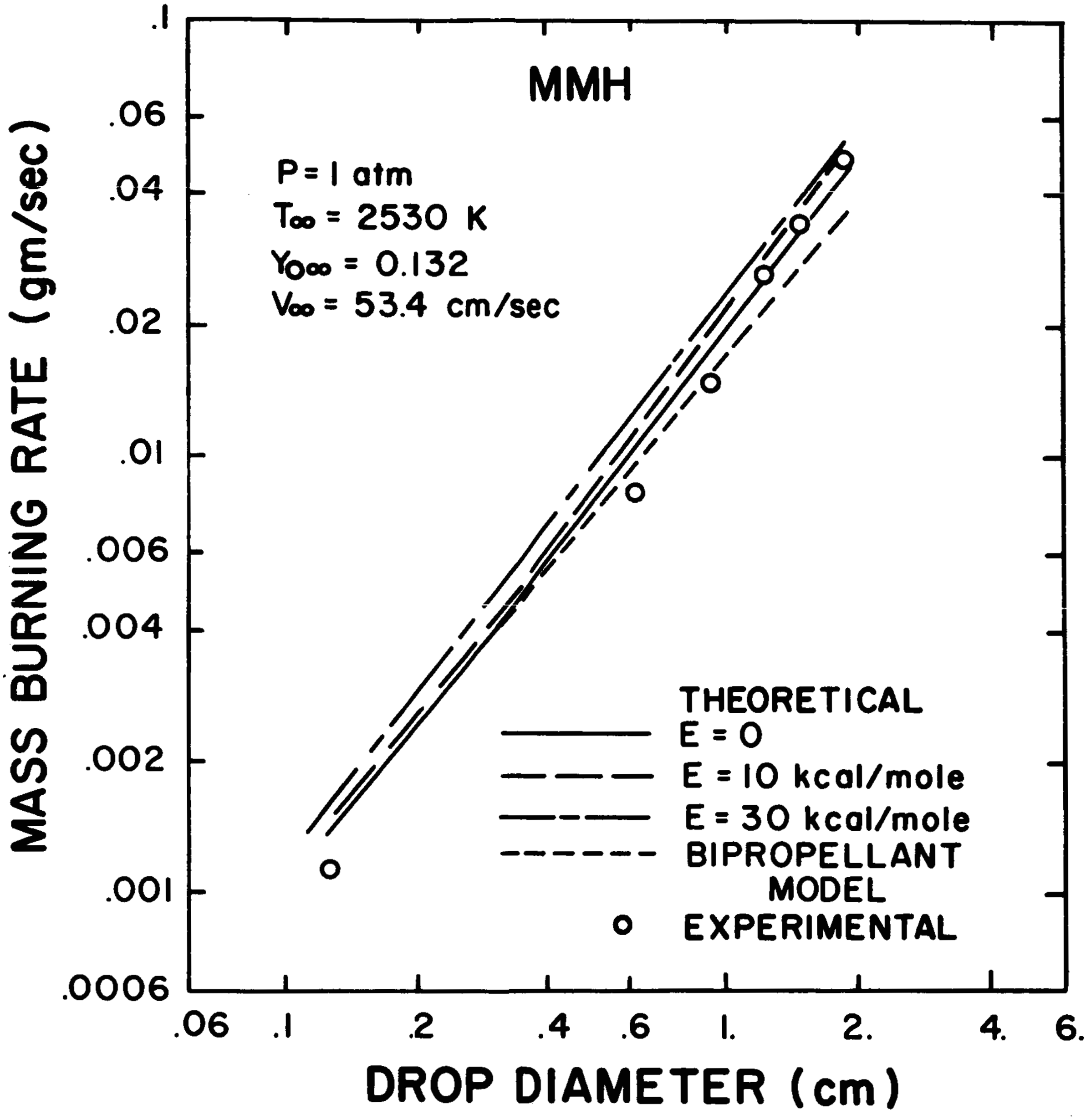

Figure 8 MMH Burning Rates at a Typical Oxidation Condition for Various Drop Diameters

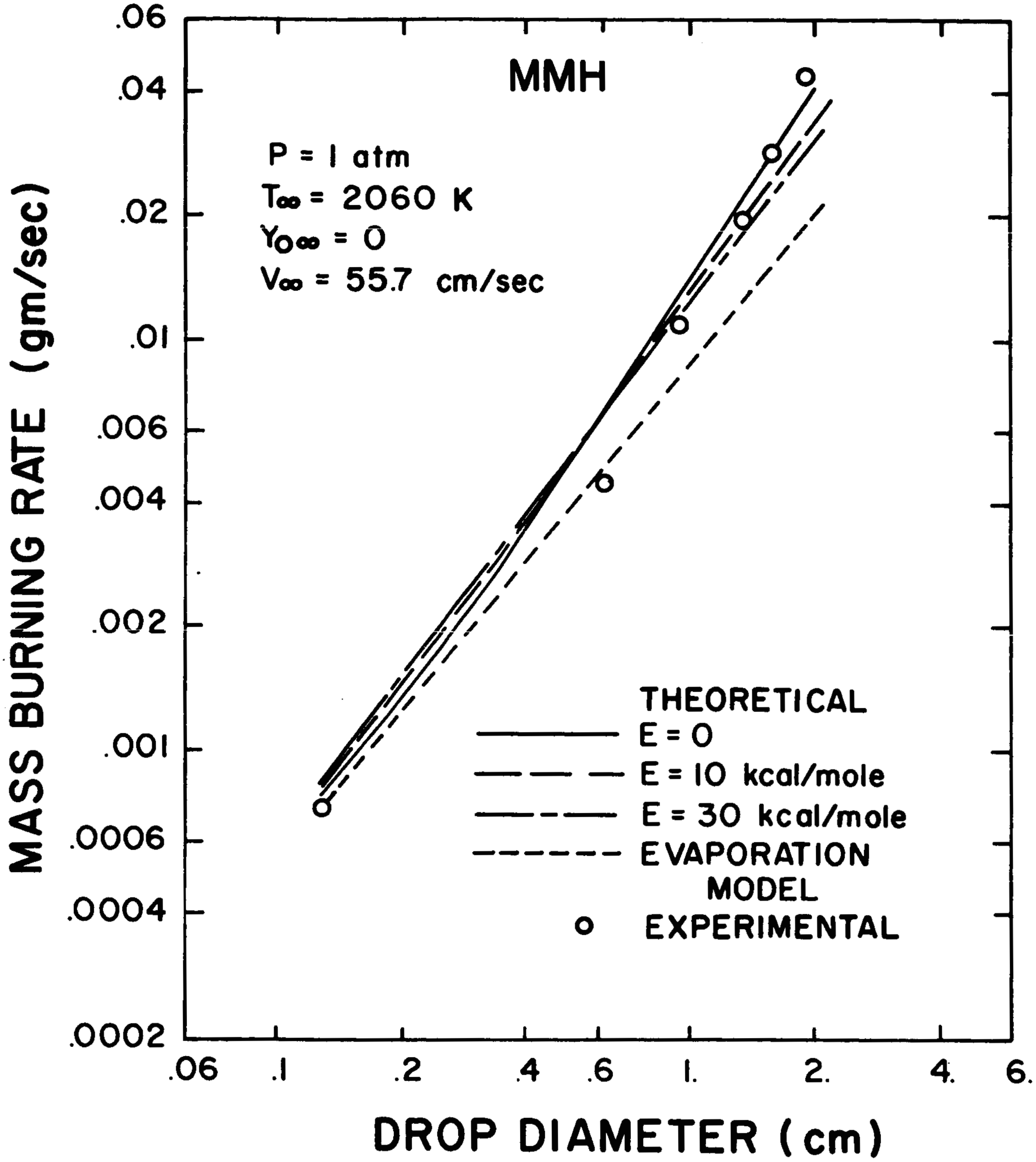

Figure 9 MMH Burning Rates at a Typical Decomposition Condition for Various Drop Diameters

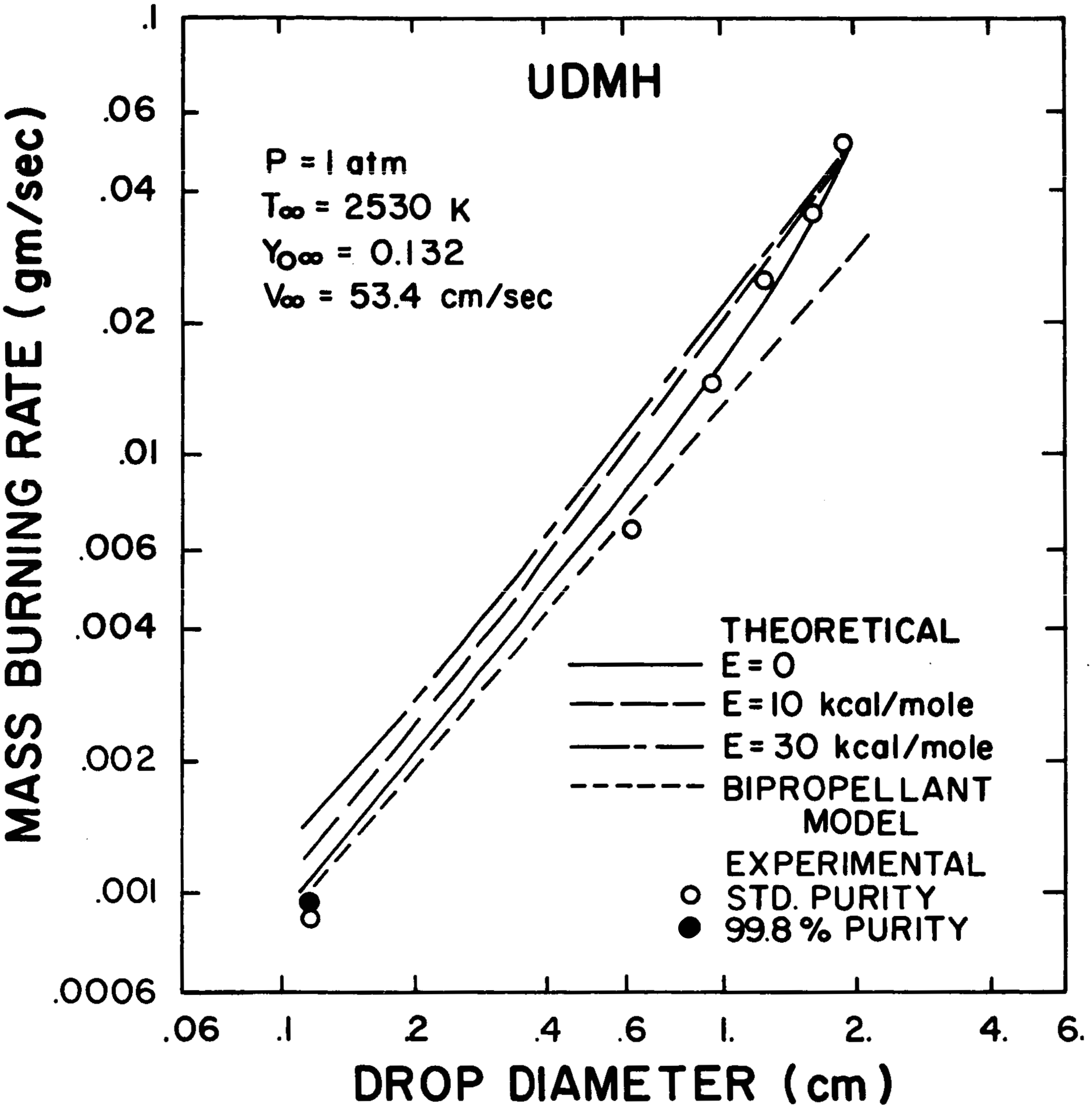

Figure 10 UDMH Burning Rates at a Typical Oxidation Condition for Various Drop Diameters

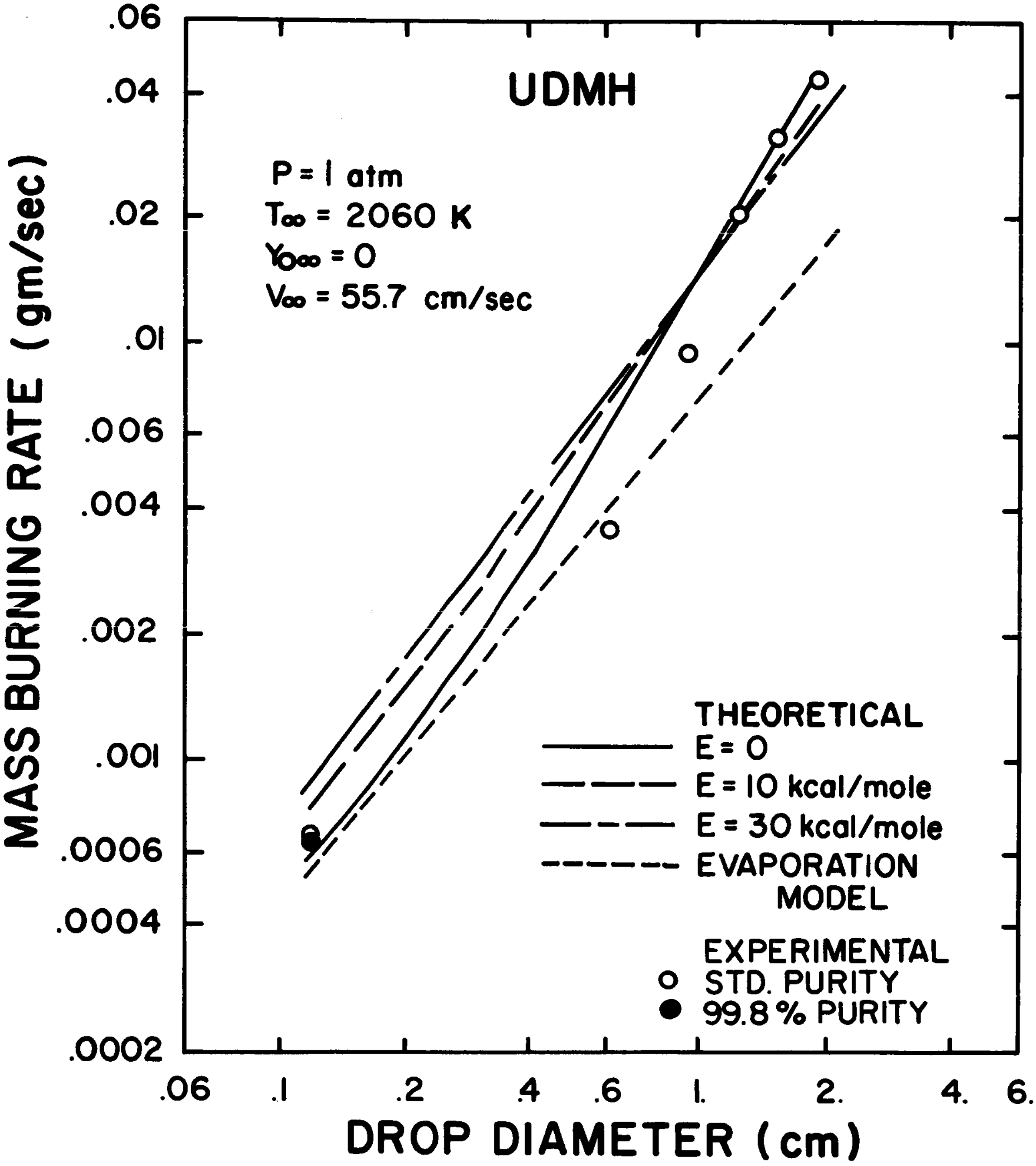

Figure 11 UDMH Burning Rates at a Typical Decomposition Condition for Various Drop Diameters

Once again, the zero activation energy solution predicts the trend in the data better than a temperature dependent laminar flame velocity solution.

One should note that in determining the value of the heat of reaction of the oxidation flame, q_2, dissociation effects were not considered. The computed bipropellant flame temperatures were as high as 5500 K. At these high temperatures dissociation will occur. If dissociation effects had been considered, the computed bipropellant flame temperatures would have been reduced, and; therefore, the computed mass burning rates would have been even lower for the bipropellant model. Lazar (24) found that computed bipropellant burning rates were as much as 50% higher than experimental values for his conditions unless dissociation effects were considered. Since dissociation effects are not a factor in the evaporation model for decomposition conditions, the apparent superiority of the bipropellant model over the evaporation model could thus be explained.

4.3 Effect of Ambient Oxygen Concentration

The effect of various ambient oxygen concentrations on the burning rates of the three fuels was also investigated using both the suspended droplet and porous sphere techniques. Figures 12, 13, and 14 summarize the results for three drop diameters and for the three fuels.

As indicated on Figure 12, as diameter increased, the effect of increasing ambient oxygen concentration decreased. The bipropellant solution for hydrazine is not shown for clarity; in all cases, the bipropellant solution predicted mass burning rates lower than

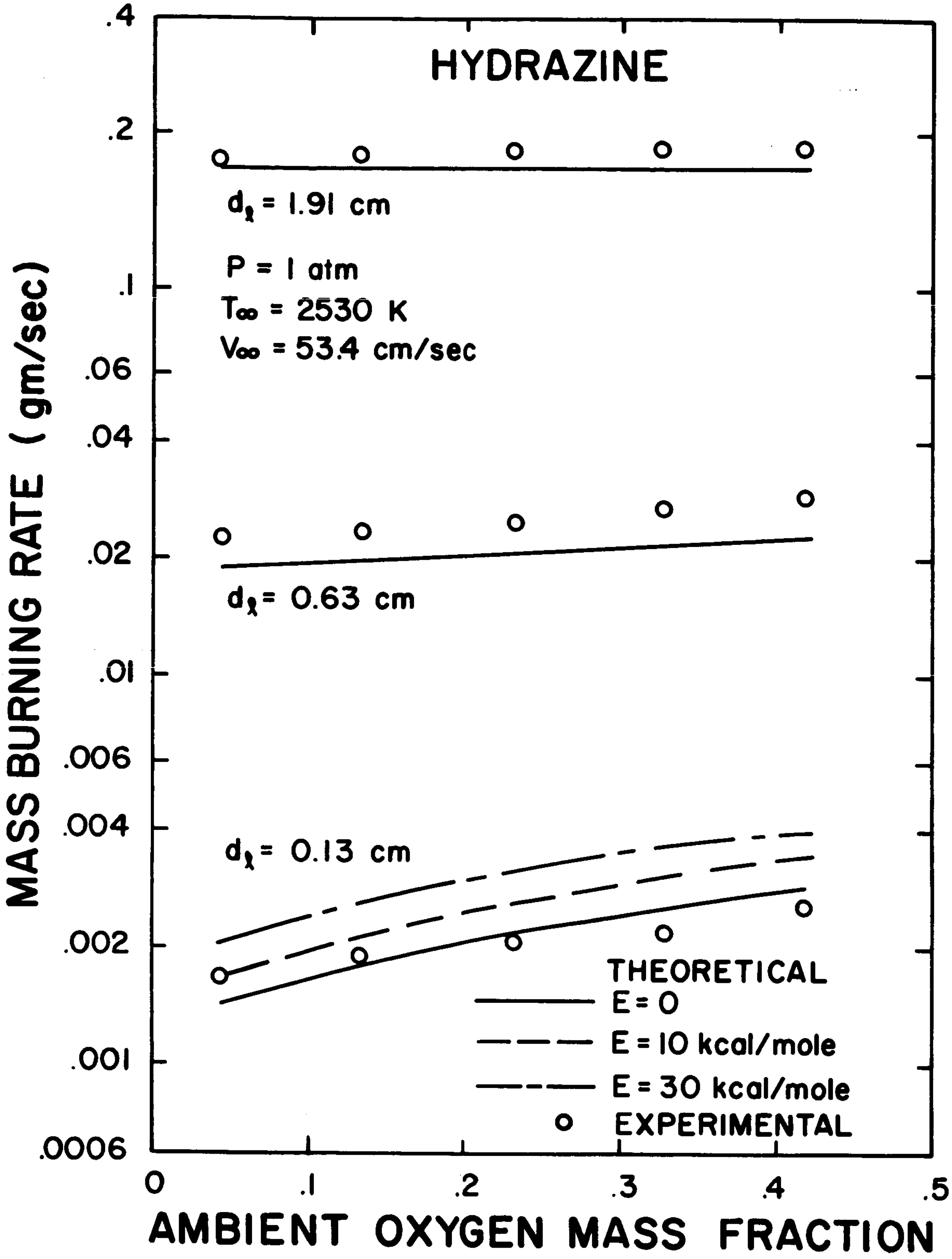

Figure 12 Hydrazine Burning Rates at Various Ambient Oxygen Concentrations

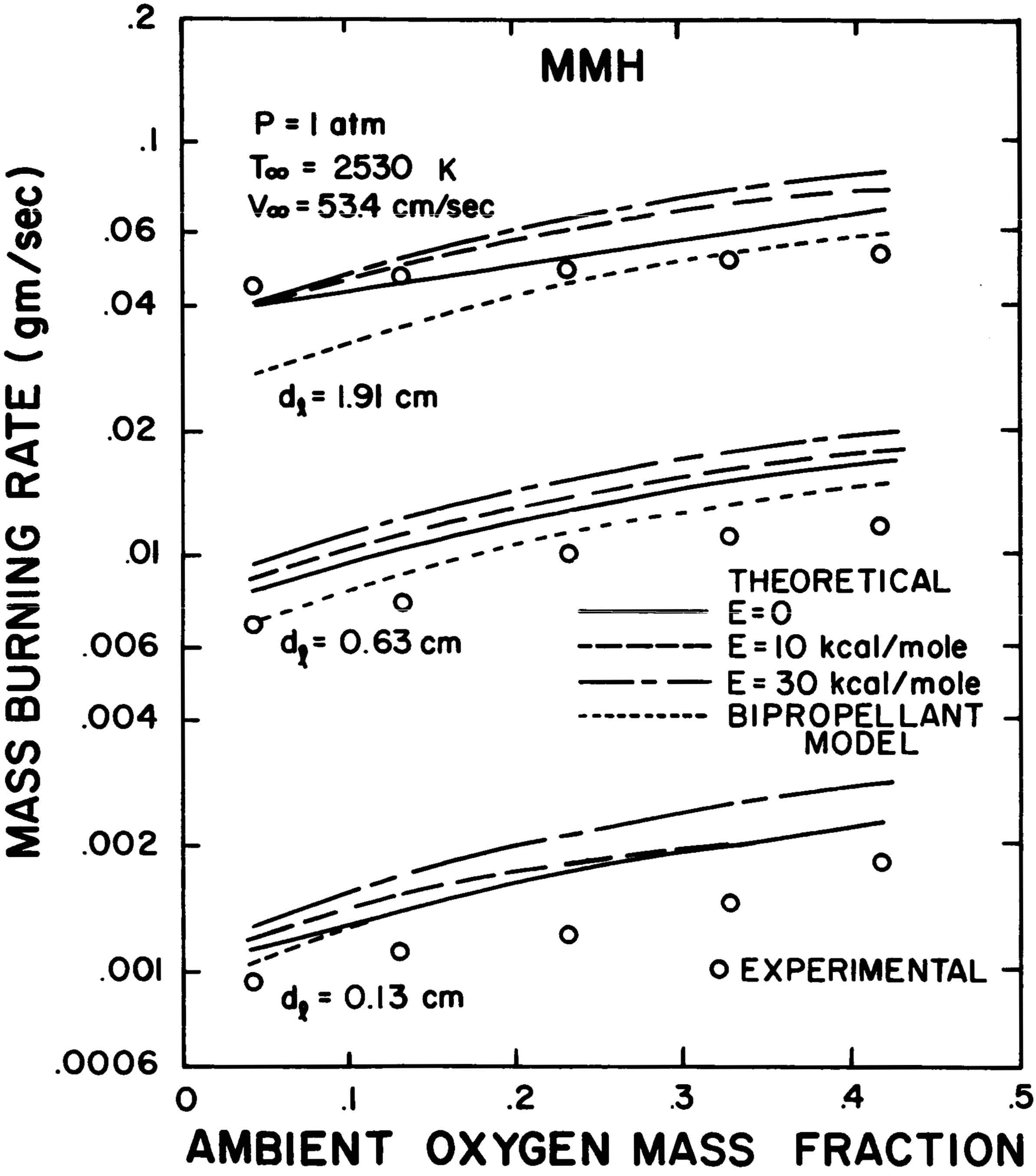

Figure 13 MMH Burning Rates at Various Ambient Oxygen Concentrations

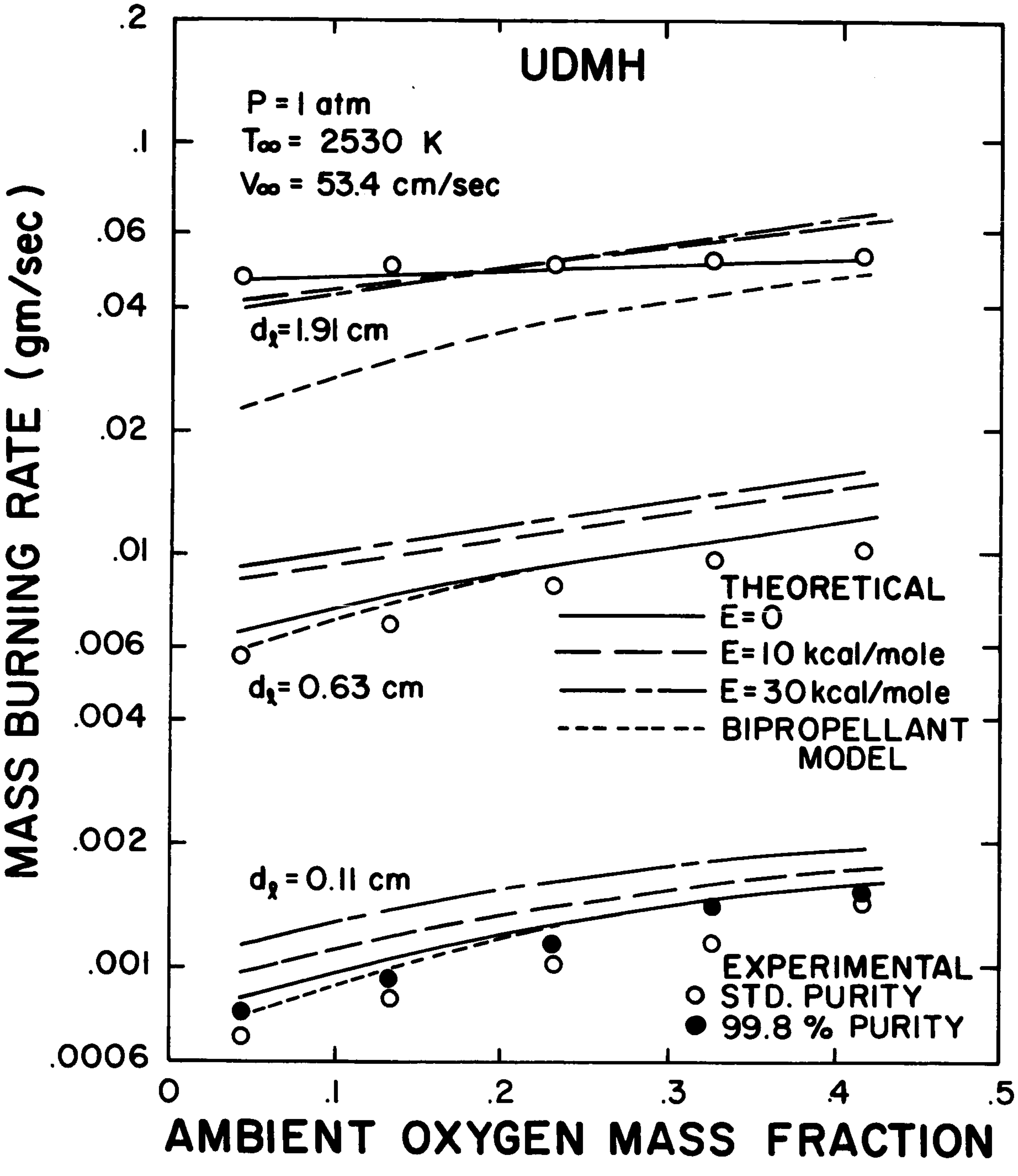

Figure 14 UDMH Burning Rates at Various Ambient Oxygen Concentrations

experimental values. Here again, the hybrid zero activation energy solution predicts the trends in the data best.

The bipropellant solution is shown on Figure 13 for MMH since it predicts the data as well as or better than the hybrid solution. However, as indicated previously, including dissociation effects would lower the predicted bipropellant burning rates. Just as for hydrazine, the effect of increasing ambient oxygen concentration decreased as drop diameter increased.

Similar behavior was found for UDMH as illustrated on Figure 14. Note that the 99.8% purity UDMH consistently yielded higher burning rates than the standard purity UDMH for the small diameter results. The high purity UDMH was only tested at the small diameter condition.

4.4 Effect of Ambient Temperature

In addition to the oxidation results, decomposition data was also obtained for the three fuels using the two experimental techniques. Figures 15, 16, and 17 summarize the results for three of the drop diameters tested.

As in the case of increasing ambient oxygen concentration, Figure 15 indicates that as drop diameter increased the effect of increasing ambient temperature decreased for hydrazine. As before, the hybrid model with E=0 gave the best correlation of the data.

For MMH, shown on Figure 16, a pure evaporation solution worked best for the two small diameters whereas the hybrid solution with E=0 worked best for the large diameter indicating the onset of monopropellant behavior.

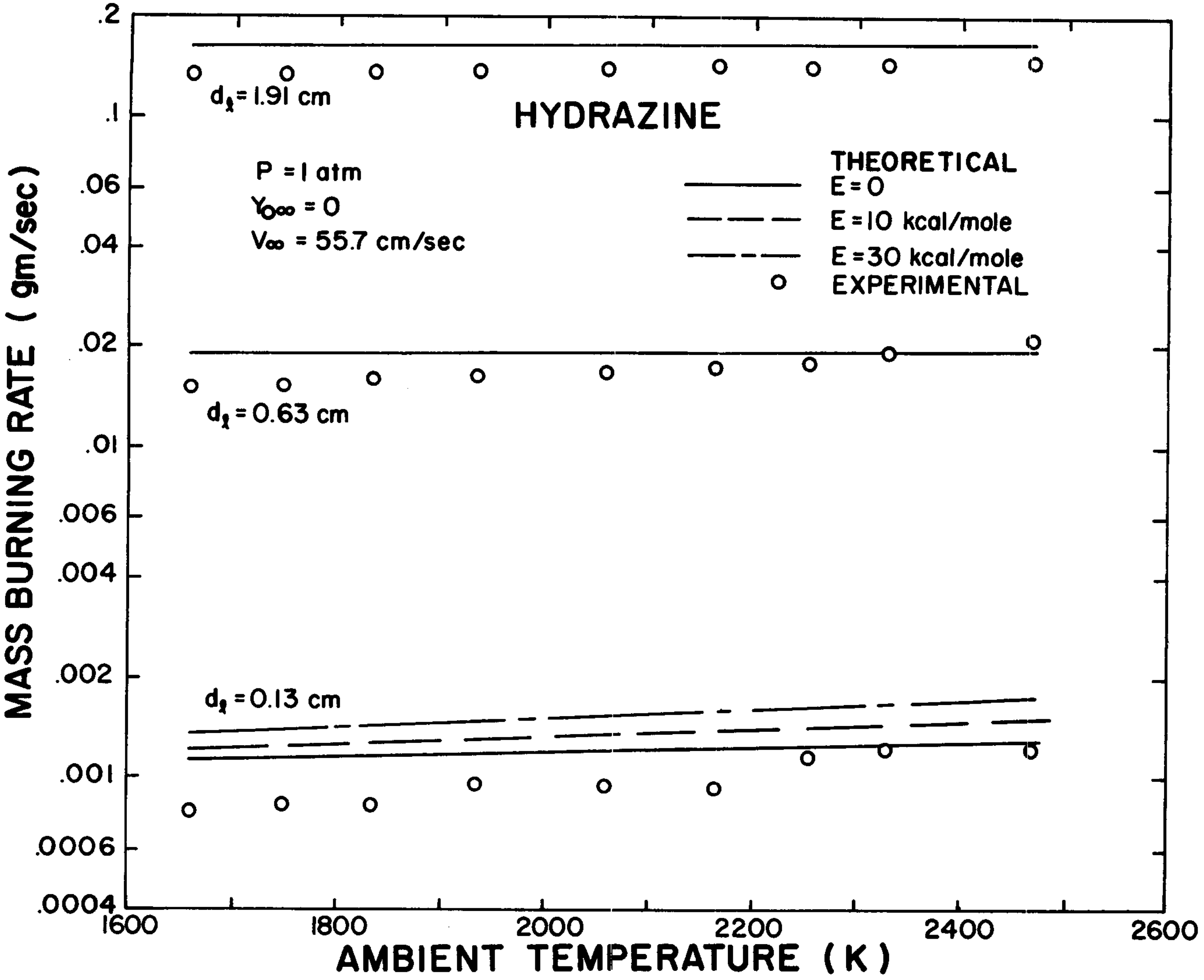

Figure 15 Hydrazine Burning Rates at Various Ambient Temperatures

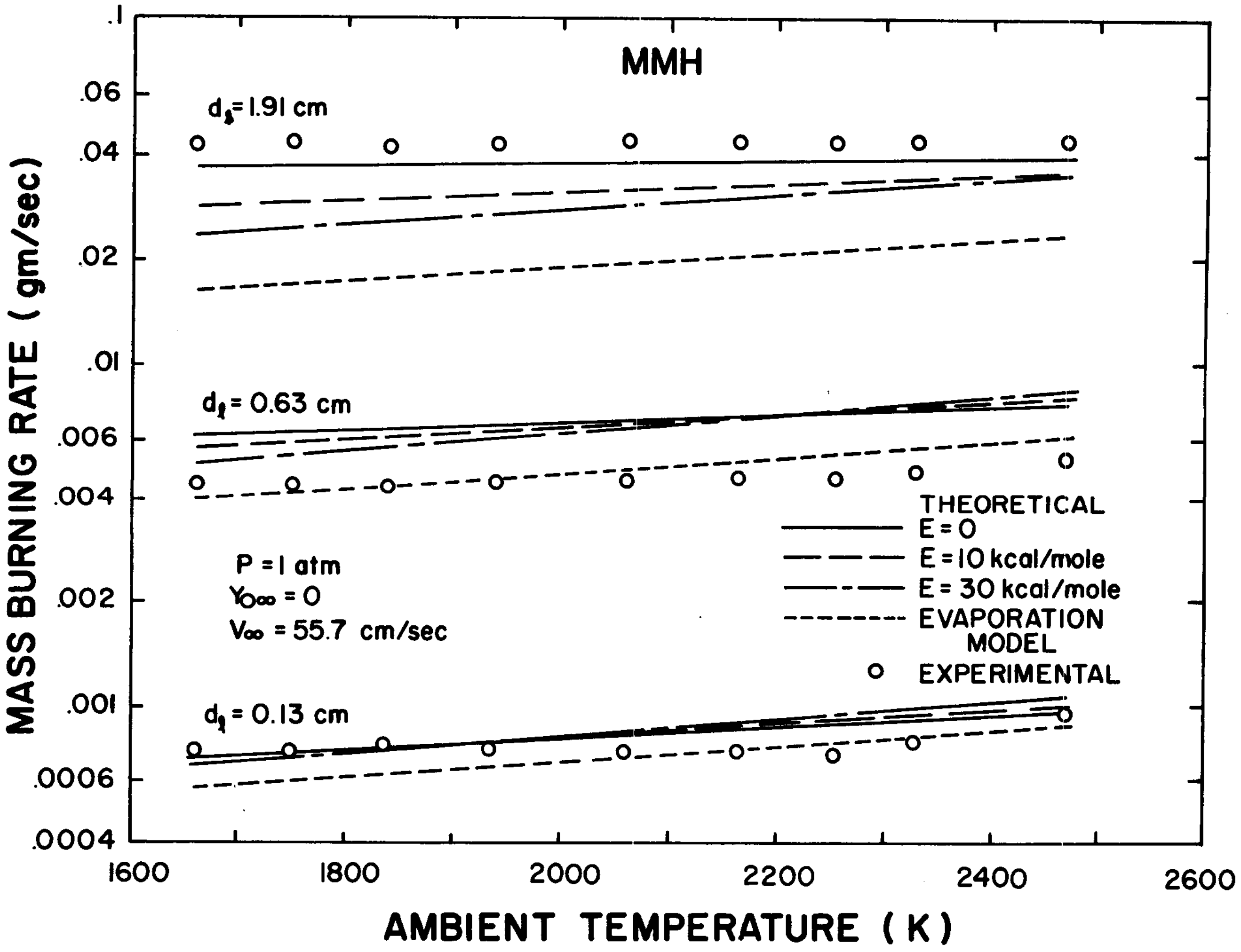

Figure 16 MMH Burning Rates at Various Ambient Temperatures

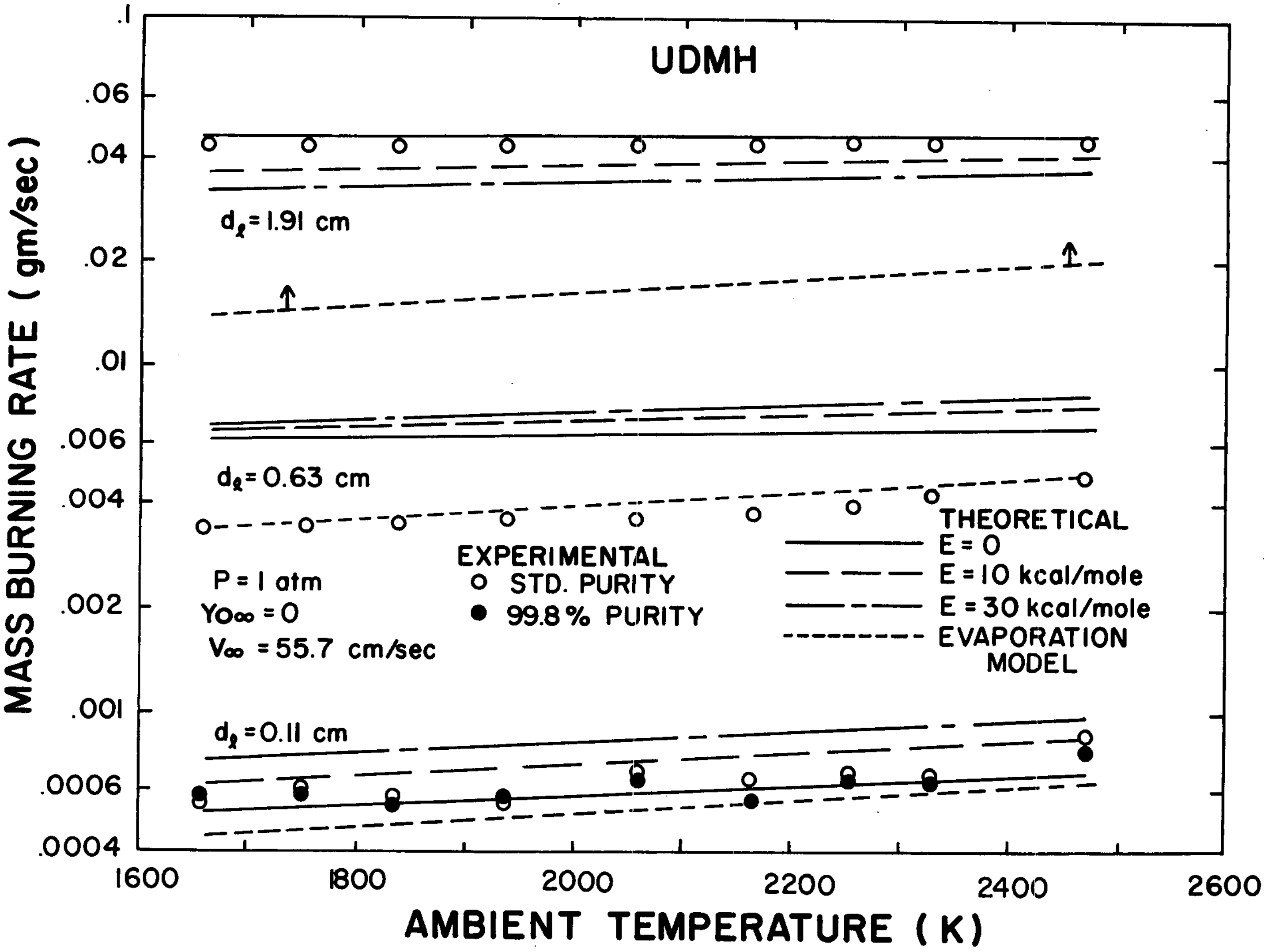

Figure 17 UDMH Burning Rates at Various Ambient Temperatures

Figure 17 illustrates similar behavior for UDMH. Note that in contrast to the oxidation conditions, the samples of different purity gave nearly the same mass burning rate at all decomposition conditions for the small diameter droplet.

4.5 Overall Comparison of Experimental Values and the Hybrid Model

In order to get a more general picture as to how well the hybrid model predicted experimental mass burning rates, a direct comparison was made as shown on Figures 18, 19, and 20 for the three fuels. Also plotted on these figures are experimental values of the burning rates of the fuels available in the literature. Since the temperature independent laminar flame velocity expression correlated the data better than a temperature dependent expression, only the temperature independent case is plotted.

The additional burning rate data plotted on Figures 18, 19, and 20 was taken from Dykema and Greene (6), Rosser (3), Lawver, et al., (8), and Kosvic and Breen (9). Since the convective conditions were not well defined for these experiments, only the influence of natural convection was considered in calculating β_∞. The Nusselt number for natural convection was calculated using the expression:

$$Nu = 2 + 0.6\ Gr^{1/4}\ Pr^{1/3} \tag{4.2}$$

The Grashof number was estimated from the following relation:

$$Gr = \frac{\rho^2\ g\ d_\ell^{\ 3}}{\mu^2} \tag{4.3}$$

suggested by Spalding (31) for burning spheres. The correlations used to determine the properties necessary to calculate the Grashof

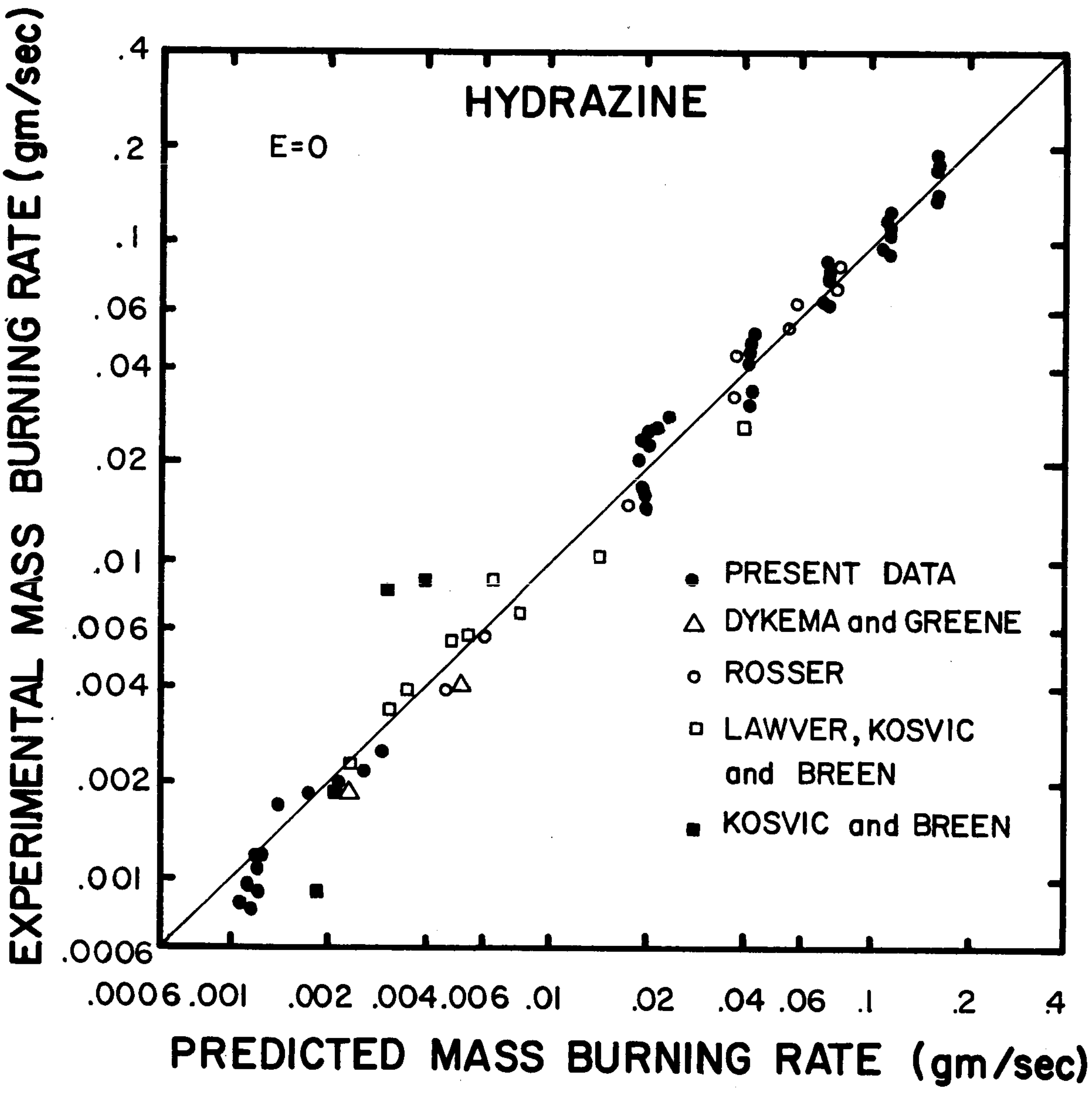

Figure 18 Experimental and Predicted Burning Rates for Hydrazine

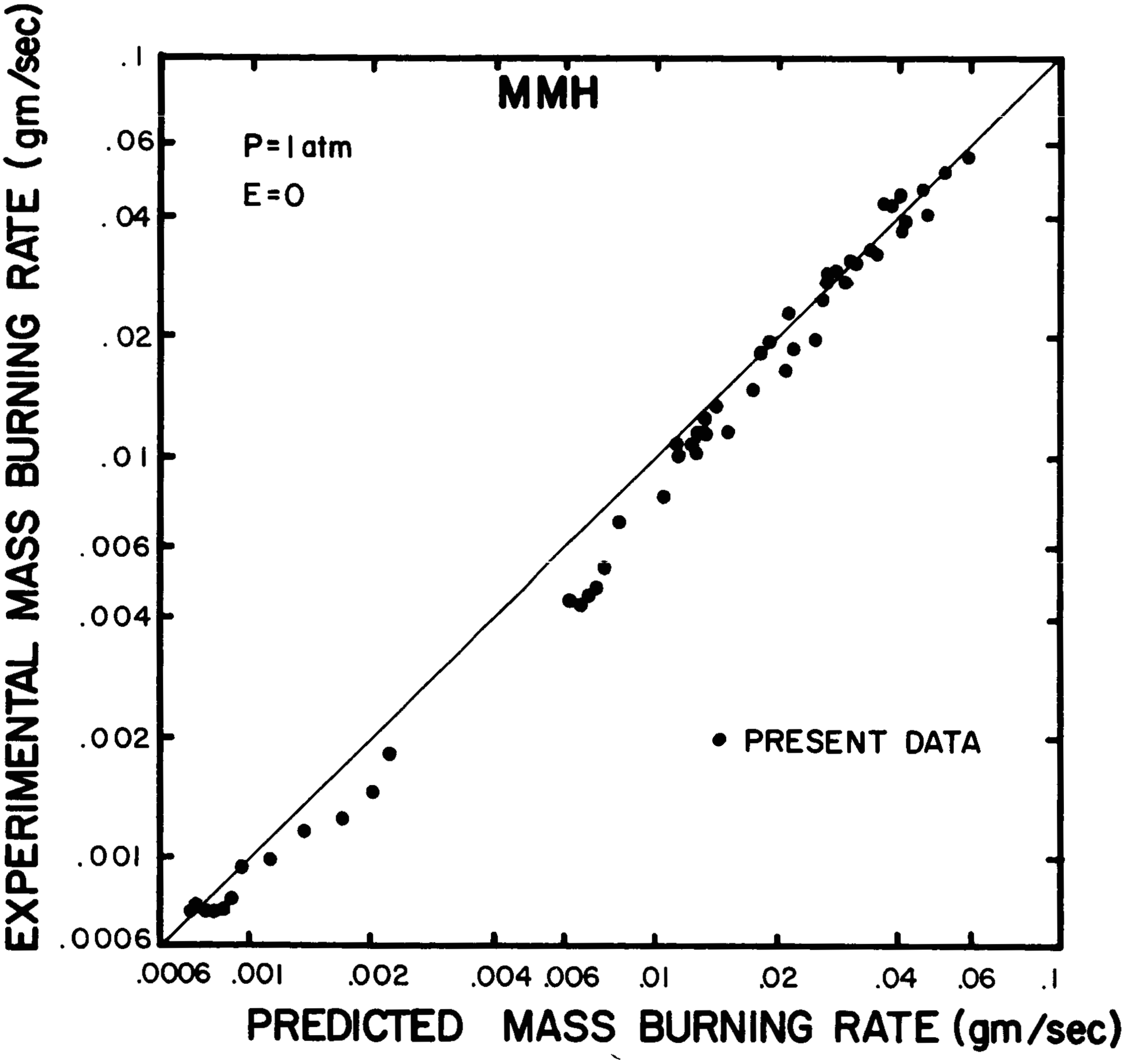

Figure 19 Experimental and Predicted Burning Rates for MMH

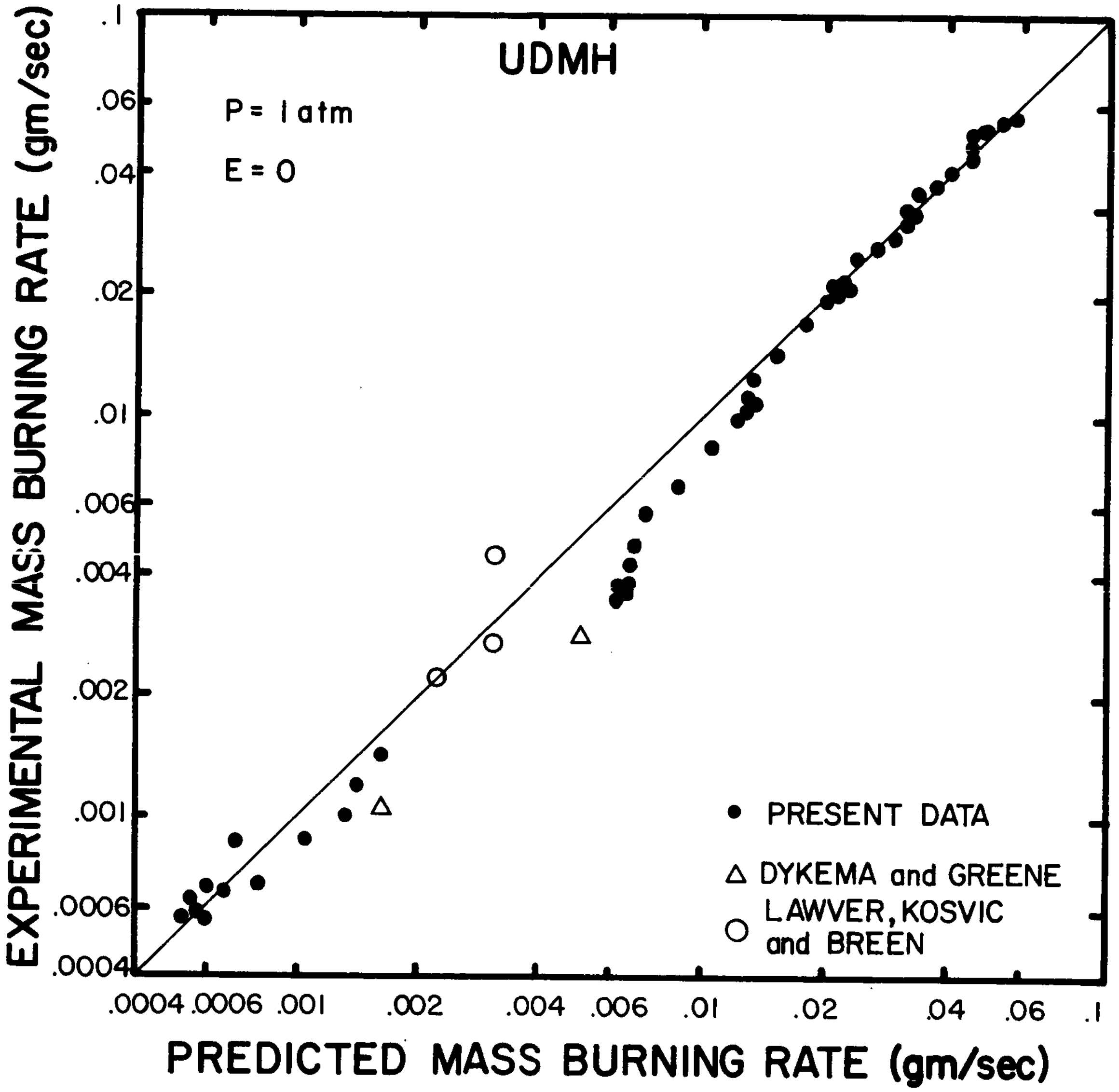

Figure 20 Experimental and Predicted Burning Rates for UDMH

and Prandtl numbers are the same as were used previously and are listed in Appendix A.

The data of Dykema and Greene (6), Rosser (5), and Lawver, et al., (8) was all taken at approximately room temperature. However, the same properties as listed in Table 2 were used in the hybrid model predictions for these low temperature conditions. In addition the same value of A as listed in Table 3 was also used.

The data of Kosvic and Breen (9) was taken at a pressure of 7.8 atm. However, the temperature was not specified for their reported results although they indicated that it was somewhere in the range of 1000 to 5500 F. The points shown in Figure 18 were computed with an ambient temperature of 2000 K since this temperature lies in about the middle of the reported range. In addition, the pre-exponential factor, A, was assumed proportional to pressure which corresponds to an overall reaction order of two as reported by Antoine (30).

A statistical analysis of the results for hydrazine plotted in Figure 18 indicated that the average percent error between predicted and experimental mass burning rates was 18.8%.

The results for MMH are shown on Figure 19. The average percent error for MMH was 17.1%.

Figure 20 shows the results for UDMH. The average error in this case was 18.7%.

CHAPTER V

SUMMARY AND CONCLUSIONS

5.1 Summary

The overall objective of the present investigation was to study the combustion characteristics of the hydrazine fuels at high temperature and atmospheric pressure. The specific objectives of the study were as follows:

1. To determine droplet burning rates as a function of ambient temperature, ambient oxygen concentration, and droplet diameter.
2. To develop a semitheoretical hybrid combustion model which provides a means of estimating the burning rates for these fuels.

The specific fuels considered in the study were hydrazine, MMH, UDMH, and A-50, however, a steady burning condition could not be achieved for A-50 for any test condition. Therefore, only results for hydrazine, MMH, and UDMH were obtained.

Two different experimental techniques were used to provide a large range of droplet sizes. The smallest diameter data was obtained using the suspended droplet technique. All other data was obtained using a porous sphere internally supplied with liquid fuel. The techniques differed in the energy required to vaporize the liquid fuel. However, theoretical considerations indicated that the measured burning rates at a given test condition would be negligibly different using the two techniques. The overall experimental range included ambient temperatures from 1660 to 2530 K, ambient oxygen mass fractions from 0.0 to 0.418, and drop sizes from 0.11 to 1.91 cm.

Spalding's thin flame approximation (16) was used as a basis in the development of a theoretical model of hybrid combustion. The model developed required kinetic parameters for solution. However, these parameters are not known for droplet combustion of the fuels of interest. Therefore, the kinetic parameters had to be computed from the experimental data at a given test condition. These same parameters were then used to predict the data at all other experimental conditions. In addition, the hybrid model with the same kinetic parameters was used to predict data available in the literature. The agreement between the predicted and experimental burning rates was quite good for the test range considered.

5.2 Conclusions

The major conclusions of the study are as follows:

1. The experimental mass burning rates of all three fuels increase slightly with increasing ambient temperature for the temperature range tested. As drop diameter increases the percent increase in mass burning rate with temperature decreases.
2. Experimental mass burning rates increase with increasing ambient oxygen concentration for all three fuels in the ambient oxygen concentration range tested. The percent increase in mass burning rate with ambient oxygen

concentration decreases with increasing drop diameter.

3. As drop diameter increases the experimental mass burning rates deviate from a bipropellant or evaporation solution indicating the onset of reactive behavior. The deviation is especially evident for hydrazine where an evaporation model predicts burning rates as much as an order of magnitude lower than observed experimental values. The deviations for MMH and UDMH are less pronounced than that for hydrazine. However, the hybrid solution does predict the trend with drop diameter better than the bipropellant model for all three fuels.
4. The hybrid correlation does predict the observed trends in mass burning rate with drop diameter, ambient temperature, and ambient oxygen concentration for all three fuels. A temperature independent laminar flame velocity expression gives the best overall correlation for all three fuels and the experimental range tested.
5. Theoretically, ambient conditions have a negligible effect on mass burning rates for strong monopropellant behavior. However, ambient conditions play an important role in bipropellant combustion.

BIBLIOGRAPHY

1. Priem, R. J., and Heidmann, M. F., "Propellant Vaporization as a Design Criteria for Rocket Engine Combustion Chambers," NASA TR-67, 1960.

2. Rosser, W. A., Jr., "The Decomposition Burning of Monopropellant Drops: Hydrazine, Nitromethane, and Ethyl Nitrate," Progress Report No. 20-305, 1957, Jet Propulsion Laboratory, Pasadena, California.

3. Rosser, W. A., Jr., and Peskin, R. L., "A Study of Decomposition Burning," Combustion and Flame, Vol. 10, June 1966, pp. 152-160.

4. del Notario, P. P., and Tarifa, C. S., "An Experimental Investigation on the Combustion of Monopropellant Droplets," TN 59-628, January 1959, Air Force Office of Scientific Research.

5. Faeth, G. M., Karhan, B. L., and Yanyecic, G. A., "Ignition and Combustion of Monopropellant Droplets," AIAA Journal, Vol. 6, No. 4, April 1968, pp. 684-689.

6. Dykema, O. W., and Greene, S. A., "An Experimental Study of RP-1, UDMH, and N_2H_4 Single Droplet Burning in Air and in Oxygen," Progress in Astronautics and Rocketing Series, Vol. 2, Academic Press, New York, 1960, pp. 299-324.

7. Lawver, B. R., "Some Observations on the Combustion of N_2H_4 Droplets," Paper No. 65-355, AIAA Second Annual Meeting, San Francisco, California, July 1965.

8. Lawver, B. R., Kosvic, T. C., and Breen, B. P., "Effects of Additives on the Combustion of Hydrazine," AFRPL-TR-67-288, January 1968, Dynamic Science Corporation, Monrovia, California.

9. Kosvic, T. C., and Breen, B. P., "Study of Additive Effects on Hydrazine Combustion and Combustion Instability at High Pressure," AFRPL-TR-69-12, November 1969, Dynamic Science Corporation, Monrovia, California.

10. Faeth, G. M., "Prediction of Pure Monopropellant Droplet Life Histories," AIAA Journal, Vol. 8, No. 7, July 1970, pp. 1308-1314.

11. Friedman, R., and Macek, A., "Ignition and Combustion of Aluminum Particles in Hot Gases," Combustion and Flame, Vol. 6, No. 1, March 1962, pp. 9-19.

12. Jones, W. H. (Chairman), JANAF Thermochemical Tables, Dow Chemical Company, Midland, Michigan.

13. Kobayasi, K., "An Experimental Study of the Combustion of a Fuel Droplet," Fifth Symposium (International) on Combustion, Reinhold, New York, 1954, pp. 141-148.

14. Lorell, J., and Wise, H., "Steady State Burning of a Liquid Droplet. I. Monopropellant Flame," The Journal of Chemical Physics, Vol. 23, No. 10, October 1955, pp. 1928-1932.

15. Williams, F. A., "Theory of the Burning of Monopropellant Droplets," Combustion and Flame, Vol. 3, December 1959, pp. 529-544.

16. Spalding, D. B., and Jain, V. K., "Theory of the Burning of Monopropellant Droplets," A.R.C. Technical Report No. 20-176, Current Paper No. 447, 1958.

17. Adler, J., and Spalding, D. B., "One-dimensional Laminar Flame Propagation with an Ehtalpy Gradient," Proc. Roy. Soc. A., Vol. 261, 1961, pp. 53-78.

18. Jain, V. K., "The Theory of Burning of Monopropellant Droplets in an Atmosphere of Inerts," Combustion and Flame, Vol. 7, March 1963, pp. 17-27.

19. Tarifa, C. S., del Notario, P. P., and Moreno, F. G., "Combustion of Liquid Monopropellants and Bipropellants in Droplets," Eighth Symposium (International) on Combustion, Williams and Wilkins, Baltimore, 1962, pp. 1035-1056.

20. Fendell, F. E., "Finite Rate Burning of a Monopropellant Droplet in a Stagnant Atmosphere," Astronautica Acta, Vol. 11, No. 6, 1965, pp. 418-421.

21. "Analysis of Liquid Rocket Engine Combustion Instability," Technical Report No. AFRPL-TR-65-254, January 1966, Dynamic Science Corporation, Monrovia, California.

22. Eberstein, I. J., and Glassman, I., "The Gas-Phase Decomposition of Hydrazine and Its Methyl Derivatives," Tenth Symposium (International) on Combustion, The Combustion Institute, Pittsburgh, 1965, pp. 365-374.

23. Faeth, G. M., "The Kinetics of Droplet Ignition in a Quiescent Air Environment," Ph.D. Thesis, 1964, The Pennsylvania State University, University Park, Pennsylvania.

24. Lazar, R. S., "Bipropellant Droplet Combustion in the Vicinity of the Critical Point," Ph.D. Thesis, 1970, The Pennsylvania State University, University Park, Pennsylvania.

25. Williams, F. A., "On the Assumptions Underlying Droplet Vaporization and Combustion Theories," The Journal of Chemical Physics, Vol. 33, No. 1, July 1960, pp. 133-144.

26. Brzustowski, T. A., "Chemical and Physical Limits on Vapor-Phase Diffusion Flames of Droplets," Canadian Journal of Chemical Engineering, Vol. 43, February 1965, pp. 30-35.

27. Williams, F. A., Combustion Theory, Addison Wesley, Reading, Massachusetts, 1965.

28. Faeth, G. M., "Flame Zone Development of Monopropellant Droplets," Combustion and Flame, Vol. 12, October 1968, pp. 411-416.

29. Combs, R. L., Discussion of paper by Eisenklam, P. S., Arunachalam, S. A., and Weston, J. A., "Evaporation Rates and Drag Resistance of Burning Drops," Eleventh Symposium (International) on Combustion, The Combustion Institute, Pittsburgh, 1967, p. 728.

30. Antoine, A. C., "The Mechanism of Burning of Liquid Hydrazine," Eighth Symposium (International) on Combustion, Williams and Wilkins, Baltimore, 1962, pp. 1057-1059.

31. Spalding, D. B., "The Combustion of Liquid Fuels," Fourth Symposium (International) on Combustion, Williams and Wilkins, Baltimore, 1953, pp. 847-864.

32. Harshman, R. C., "The Physical and Chemical Properties of the Alkyl Hydrazines," Jet Propulsion, April 1957, pp. 398-400.

33. Lewis, G. H., and Randall, M., Thermodynamics, 2nd Ed., Revised by Pitzer, K. S., and Brewer, L., McGraw-Hill, New York, 1961.

34. Scott, D. W., Oliver, G. D., Gross, M. E., Hubbard, W. N., and Huffman, H. M., "Hydrazine: Heat Capacity, Heats of Fusion and Vaporization, Vapor Pressure, Entropy and Thermodynamic Functions," Journal of the American Chemical Society, Vol. 71, July 1949, pp. 2293-2297.

35. Aston, J. G., Fink, H. L., Jang, G. J., and Russel, K. E., "The Heat Capacity, Heats of Fusion and Vaporization, Vapor Pressures, Entropy and Thermodynamic Functions of Methylhydrazine," Journal of the American Chemical Society, Vol. 73, May 1951, pp. 1939-1943.

36. Campbell, D. T., and Chadwick, W. D., "Combustion Instability Analysis at High Chamber Pressure, Final Report," AFRPL-TR-68-179, August 1968, Rocketdyne, Canoga Park, California.

37. Svehla, R. A., "Estimated Viscosities and Thermal Conductivities of Gases at High Temperatures," NASA Technical Report R-132, 1962.

38. Kobe, K. A., and Lynn, R. E., Chemical Reviews, Vol. 52, p. 117, 1963.

39. Bizjak, F., and Stai, D. F., "Temperature-Entropy Diagram of Monomethylhydrazine," AIAA Journal, Vol. 2, No. 5, May 1964, pp. 954-956.

40. "Dimazine-Unsymmetrical Dimethylhydrazine; Properties, Applications, Reactions," FMC Corporation, Inorganic Chemicals Division, New York, New York.

41. Audrieth, L. F., and Ogg, B. A., The Chemistry of Hydrazine, John Wiley and Sons, New York, 1951.

APPENDIX A

PHYSICAL PROPERTIES

A.1 References for Physical Properties

The references for the physical properties required in the calculations are shown on Table 5. The reference temperature, T°, used in the calculations was 298.15 K. The correlations used to compute properties are discussed in the following.

A.2 Gas Phase Properties

The specific heats of the fuel, fuel decomposition products, oxidizer, and bipropellant flame products were assumed constant. The temperatures at which the specific heats were evaluated were as follows: C_F was evaluated at 1000 K, C_{FP} was evacuated at 2000 K, and C_P and C_o were evaluated at 2500 K. The fuel decomposition products and bipropellant flame products were treated as a single species for these calculations.

The bipropellant flame products were taken as those determined from the stoichiometric combustion of the fuel in oxygen. However, the products of fuel decomposition cannot be determined in such an easy manner. For hydrazine, the fuel decomposition products were taken to be those as suggested by Andrieth and Ogg (41); namely

$$N_2H_4 = 0.50\ NH_3 + 0.25\ N_2 + 0.25\ H_2 \qquad (A.1)$$

The decomposition products for MMH and UDMH were calculated at the adiabatic decomposition flame temperature allowing for all relevant

Table 5

References for Physical Properties of the Fuels

	References			
Property	N_2H_4	MMH	UDMH	Combustion Products and Ambient Gas
T_ℓ	32	32	32	--
L	32	32	32	--
ΔH°	32	32	32	33
C	34	35	36	37
λ	37[a]	37[a]	37[a]	37
T_d[b]	38	39	40	--
P_d[b]	38	39	40	--

[a] Computed, Method of Reference (37).

[b] Required for the Computation of λ, Method of Reference (37).

dissociation reactions. The main products of decomposition were used for property calculations. These were as follows:

$$\text{MMH} = 0.33\ H_2 + 0.33\ N_2 + 0.33\ CH_4 \qquad (A.2)$$

$$\text{UDMH} = 0.50\ CH_4 + 0.25\ N_2 + 0.15\ H_2 + 0.10\ HCN \qquad (A.3)$$

The thermal conductivity of Region j of Figure 3 was assumed to vary linearly with temperature, that is

$$\lambda_j = \lambda_{j\ell}(T/T_\ell) \qquad (A.4)$$

where $\lambda_{j\ell}$ represents the thermal conductivity of the gas mixture evaluated at temperature T_ℓ for Region j. The constants $\lambda_{j\ell}$ were evaluated by considering the possible limits of the thermal conductivity in each region. For example, hydrogen, ammonia, and methane have somewhat higher thermal conductivities than gaseous species such as carbon dioxide, nitrogen, and oxygen. Therefore, large quantities of hydrogen in a region would raise the thermal conductivity over the corresponding value of the thermal conductivity for no hydrogen present.

By considering the possible species present in each region, a high and low value of $\lambda_{j\ell}$ was determined. The $\lambda_{j\ell}$ used in the calculations was the average of the high and low values.

A.3 Ambient Gas Properties

The Reynolds number, Prandtl number, and Grashof number appearing in the convection correction equations, Equations (3.55) and (4.2), were evaluated for the ambient gas mixture. The properties appearing in these dimensionless numbers were evaluated as follows for an N component gas mixture:

Specific Heat

$$C = \sum_{i=1}^{N} X_i\ M_i\ C_i / \sum_{i=1}^{N} X_i\ M_i \qquad (A.5)$$

where

$$C_i = B_1 + B_2\ T_\infty \qquad \text{(cal/gm-K)} \qquad (A.6)$$

Viscosity

$$\mu = \sum_{i=1}^{N} X_i\ \mu_i \qquad (A.7)$$

where

$$\mu_i = B_3 + B_4\ T_\infty \qquad \text{(gm/cm-sec)} \qquad (A.8)$$

Thermal Conductivity

$$\lambda = \sum_{i=1}^{N} X_i\ \lambda_i \qquad (A.9)$$

where

$$\lambda_i = B_5 + B_6\ T_\infty \qquad \text{(cal/cm-sec-K)} \qquad (A.10)$$

Density

$$\rho = P \sum_{i=1}^{N} X_i\ M_i / RT_\infty \qquad \text{(gm/cc)} \qquad (A.11)$$

The constants, B_1 to B_6, were determined by Lazar (24) and are tabulated in Table 6 for the species present in the ambient gas mixture.

Table 6

Constants in the Ambient Gas Property Equations[a]

Component	B_1	B_2 x10^5	B_3 x10^4	B_4 x10^7	B_5 x10^5	B_6 x10^7
O_2	0.248	1.67	2.02	2.73	4.55	1.322
O	0.282	1.67	1.85	2.50	7.18	1.282
N_2	0.282	1.21	1.52	2.35	3.18	1.232
NO	0.277	0.72	1.95	2.55	3.70	1.321
CO_2	0.298	1.35	1.52	2.35	1.19	1.397
CO	0.292	0.85	1.63	2.35	3.20	1.282

[a] From Lazar (24).

APPENDIX B

EXPERIMENTAL DATA

Table 7

Experimental Evaporation Constants and Mass Burning Rates for Hydrazine Obtained Using the Suspended Droplet Technique

$d_{\ell} = 0.13$ cm; $\rho_{\ell} = 1.00$ gm/cm^3

T_∞ (K)	$Y_{O\infty}$	V_∞ (cm/sec)	$K\times10^3$ (cm^2/sec)	$\dot{M}\times10^3$ (gm/sec)
2530	0.043	53.4	17.03	1.70
2530	0.132	53.4	19.03	1.90
2530	0.233	53.4	20.84	2.08
2530	0.328	53.4	22.06	2.21
2530	0.418	53.4	25.48	2.55
2470	0	55.7	12.36	1.24
2330	0	55.7	12.31	1.23
2255	0	55.7	11.34	1.13
2165	0	55.7	9.24	0.92
2060	0	55.7	9.52	0.95
1935	0	55.7	9.70	0.97
1835	0	55.7	8.17	0.82
1750	0	55.7	8.40	0.84
1660	0	55.7	8.02	0.80

Table 8

Experimental Evaporation Constants and Mass Burning Rates for MMH Obtained Using the Suspended Droplet Technique

$d_\ell = 0.13$ cm; $\rho_\ell = 0.87$ gm/cm^3

T_∞ (K)	$Y_{O\infty}$	V_∞ (cm/sec)	$K\times10^3$ (cm^2/sec)	$\dot{M}\times10^3$ (gm/sec)
2530	0.043	53.4	11.36	0.99
2530	0.132	53.4	13.13	1.14
2530	0.233	53.4	14.48	1.26
2530	0.328	53.4	16.80	1.46
2530	0.418	53.4	20.84	1.82
2470	0	55.7	10.97	0.96
2330	0	55.7	9.23	0.80
2255	0	55.7	8.49	0.74
2165	0	55.7	8.61	0.75
2060	0	55.7	8.51	0.74
1935	0	55.7	8.63	0.75
1835	0	55.7	8.74	0.76
1750	0	55.7	8.61	0.75
1660	0	55.7	8.70	0.76

Table 9

Experimental Evaporation Constants and Mass Buring Rates for Standard Purity UDMH Obtained Using the Suspended Droplet Technique

$d_\ell = 0.11$ cm; $\rho_\ell = 0.78$ gm/cm^3

T_∞ (K)	$Y_{O\infty}$	V_∞ (cm/sec)	$K\times10^3$ (cm^2/sec)	$\dot{M}\times10^3$ (gm/sec)
2530	0.043	53.4	9.72	0.68
2530	0.132	53.4	12.33	0.87
2530	0.233	53.4	14.44	1.01
2530	0.328	53.4	16.83	1.18
2530	0.418	53.4	20.25	1.42
2470	0	55.7	12.43	0.87
2330	0	55.7	9.26	0.65
2255	0	55.7	9.39	0.66
2165	0	55.7	8.98	0.63
2060	0	55.7	9.23	0.65
1935	0	55.7	7.93	0.56
1835	0	55.7	8.29	0.58
1750	0	55.7	8.70	0.61
1660	0	55.7	8.02	0.56

Table 10

Experimental Evaporation Constants and Mass Burning Rates for 99.8% Purity UDMH Obtained Using the Suspended Droplet Technique

$d_\ell = 0.11$ cm; $\rho_\ell = 0.78$ gm/cm^3

T_∞ (K)	$Y_{O\infty}$	V_∞ (cm/sec)	$K\times10^3$ (cm^2/sec)	$\dot{M}\times10^3$ (gm/sec)
2530	0.043	53.4	11.34	0.80
2530	0.132	53.4	13.88	0.97
2530	0.233	53.4	16.86	1.19
2530	0.328	53.4	20.35	1.43
2530	0.418	53.4	20.67	1.45
2470	0	55.7	10.49	0.76
2330	0	55.7	9.03	0.63
2255	0	55.7	9.16	0.65
2165	0	55.7	7.91	0.56
2060	0	55.7	8.92	0.63
1935	0	55.7	8.12	0.57
1835	0	55.7	8.21	0.58
1750	0	55.7	7.97	0.56
1660	0	55.7	8.02	0.56

Table 11

Experimental Mass Burning Rates Obtained Using the Porous Sphere Technique

T_∞ (K)	$Y_{O\infty}$	V_∞ (cm/sec)	d_ℓ (cm)	$\dot{M}x10^3$ (gm/sec)		
				N_2H_4	MMH	UDMH
2530	0.043	53.4	0.63	23.1	7.04	5.82
2530	0.132	53.4	0.63	24.0	8.03	6.76
2530	0.233	53.4	0.63	25.5	10.3	8.31
2530	0.328	53.4	0.63	27.0	11.4	9.75
2530	0.418	53.4	0.63	29.0	12.0	10.6
2470	0	55.7	0.63	21.2	5.35	4.84
2330	0	55.7	0.63	19.4	4.88	4.28
2255	0	55.7	0.63	18.2	4.70	4.00
2165	0	55.7	0.63	17.5	4.68	3.74
2060	0	55.7	0.63	16.9	4.56	3.60
1935	0	55.7	0.63	16.5	4.50	3.60
1835	0	55.7	0.63	16.2	4.45	3.54
1750	0	55.7	0.63	15.6	4.45	3.48
1660	0	55.7	0.63	15.1	4.45	3.42
2530	0.043	53.4	0.95	43.8	13.5	12.3
2530	0.132	53.4	0.95	45.2	14.8	14.1
2530	0.233	53.4	0.95	47.0	16.6	17.2
2530	0.328	53.4	0.95	49.8	18.8	19.8
2530	0.418	53.4	0.95	52.4	20.4	21.4
2470	0	55.7	0.95	42.0	12.5	11.1
2330	0	55.7	0.95	39.0	11.7	10.5
2255	0	55.7	0.95	36.8	11.3	10.1
2165	0	55.7	0.95	35.0	11.1	9.82
2060	0	55.7	0.95	33.6	10.8	9.51
1935	0	55.7	0.95	33.0	10.8	9.50
1835	0	55.7	0.95	32.8	10.6	9.33
1750	0	55.7	0.95	32.4	10.6	9.33
1660	0	55.7	0.95	31.8	10.4	9.10
2530	0.043	53.4	1.27	75.6	23.8	22.3
2530	0.132	53.4	1.27	77.7	26.0	25.1
2530	0.233	53.4	1.27	80.0	27.2	26.6
2530	0.328	53.4	1.27	83.0	30.8	28.8
2530	0.418	53.4	1.27	88.5	33.1	31.2
2470	0	55.7	1.27	74.5	20.5	21.8
2330	0	55.7	1.27	71.8	20.1	21.0
2255	0	55.7	1.27	68.7	19.7	20.6
2165	0	55.7	1.27	66.2	19.5	20.4
2060	0	55.7	1.27	66.2	19.3	20.3

Table 11 (Continued)

T_∞ (K)	$Y_{O\infty}$	V_∞ (cm/sec)	d_ℓ (cm)	$\dot{M}x10^3$ (gm/sec)		
				N_2H_4	MMH	UDMH
1935	0	55.7	1.27	64.7	19.1	20.1
1835	0	55.7	1.27	63.2	19.1	19.9
1750	0	55.7	1.27	63.2	18.7	19.9
1660	0	55.7	1.27	62.3	18.5	19.7
2530	0.043	53.4	1.59	112.	31.9	33.2
2530	0.132	53.4	1.59	114.	34.0	35.8
2530	0.233	53.4	1.59	116.	37.1	37.8
2530	0.328	53.4	1.59	120.	40.0	40.8
2530	0.418	53.4	1.59	124.	42.0	43.3
2470	0	55.7	1.59	108.	30.6	32.5
2330	0	55.7	1.59	104.	30.1	32.2
2255	0	55.7	1.59	101.	29.4	31.8
2165	0	55.7	1.59	99.8	29.1	31.5
2060	0	55.7	1.59	96.7	28.9	31.5
1935	0	55.7	1.59	94.5	28.9	31.2
1835	0	55.7	1.59	94.2	28.7	30.8
1750	0	55.7	1.59	92.1	28.6	30.6
1660	0	55.7	1.59	91.5	28.4	30.6
2530	0.043	53.4	1.91	172.	45.6	48.5
2530	0.132	53.4	1.91	175.	48.1	50.6
2530	0.233	53.4	1.91	180.	50.4	52.0
2530	0.328	53.4	1.91	182.	53.2	53.8
2530	0.418	53.4	1.91	186.	55.8	55.5
2470	0	55.7	1.91	145.	44.5	44.8
2330	0	55.7	1.91	142.	44.2	44.6
2255	0	55.7	1.91	140.	44.2	44.2
2165	0	55.7	1.91	140.	44.0	44.0
2060	0	55.7	1.91	138.	44.0	43.8
1935	0	55.7	1.91	138.	43.8	43.8
1835	0	55.7	1.91	137.	43.8	43.7
1750	0	55.7	1.91	135.	43.6	43.7
1660	0	55.7	1.91	135.	43.6	43.5

REPORT DISTRIBUTION LIST OF CONTRACT NO. NGR 39-009-077

Dr. R. J. Priem MS 500-209
NASA Lewis Research Center
21000 Brookpark Road
Cleveland, Ohio 44135 (2)

Norman T. Musial
NASA Lewis Research Center
21000 Brookpark Road
Cleveland, Ohio 44135

Library (2)
NASA Lewis Research Center
21000 Brookpark Road
Cleveland, Ohio 44135

Report Control Office
NASA Lewis Research Center
21000 Brookpark Road
Cleveland, Ohio 44135

Brooklyn Polytechnic Institute
Attn: V. D. Agosta
Long Island Graduate Center
Route 110
Farmingdale, New York 11735

Chemical Propulsion Information Agency
Johns Hopkins University/APL
Attn: T. W. Christian
8621 Georgia Avenue
Silver Spring, Maryland 20910

NASA
Lewis Research Center
Attn: E. W. Conrad, MS 500-204
21000 Brookpark Road
Cleveland, Ohio 44135

North American Rockwell Corporation
Rocketdyne Division
Attn: T. A. Coultas, D/991-350
Zone 11
6633 Canoga Avenue
Canoga Park, California 91304

National Technical Information Service
Springfield, Virginia 22151

Aerospace Corporation
Attn: O. W. Dykema
Post Office Box 95085
Los Angeles, California 90045

Ohio State University
Department of Aeronautical and
Astronautical Engineering
Attn: R. Edse
Columbus, Ohio 43210

TRW Systems
Attn: G. W. Elverum
One Space Park
Redondo Beach, California 90278

Bell Aeropsace Company
Attn: T. F. Ferger
Post Office Box 1
Mail Zone J-81
Buffalo, New York 14205

Pratt & Whitney Aircraft
Florida Research & Development
Center
Attn: G. D. Garrison
Post Office Box 710
West Palm Beach, Florida 33402

NASA
Lewis Research Center
Attn: L. Gordon, MS 500-209
21000 Brookpark Road
Cleveland, Ohio 44135

Purdue University
School of Mechanical Engineering
Attn: R. Goulard
Lafayette, Indiana 47907

Air Force Office of Scientific
Research
Chief Propulsion Division
Attn: Lt. Col. R. W. Haffner (NAE)
1400 Wilson Boulevard
Arlington, Virginia 22209

University of Illinois
Aeronautics/Astronautic Engineering
Department
Attn: R. A. Strehlow
Transportation Building, Room 101
Urbana, Illinois 61801

NASA
Manned Spacecraft Center
Attn: J. G. Thibadaux
Houston, Texas 77058

Massachusetts Institute of Technology
Department of Mechanical Engineering
Attn: T. Y. Toong
77 Massachusetts Avenue
Cambridge, Massachusetts 02139

Illinois Institute of Technology
Attn: T. P. Torda
Room 200 M. H.
3300 S. Federal Street
Chicago, Illinois 60616

AFRPL
Attn: R. R. Weiss
Edwards, California 93523

U. S. Army Missile Command
AMSMI-RKL, Attn: W. W. Wharton
Redstone Arsenal, Alabama 35808

University of California
Aerospace Engineering Department
Attn: F. A. Williams
Post Office Box 109
LaJolla, California 92037

Georgia Institute of Technology
Aerospace School
Attn: B. T. Zinn
Atlanta, Georgia 30332

Marshall Industries
Dynamic Science Division
Attn: L. Zung
2400 Michelson Drive
Irvine, California 92664

Mr. Donald H. Dahlene
U.S. Army Missile Command
Research, Development, Engineering
and Missile Systems Laboratory
Attn: AMSMI-RK
Redstone Arsenal, Alabama 35809

TISIA
Defense Documentation Center
Cameron Station
Building 5
5010 Duke Street
Alexandria, Virginia 22314

Office of Assistant Director
(Chemical Technician)
Office of the Director of Defense
Research and Engineering
Washington, D. C. 20301

D. E. Mock
Advanced Research Projects Agency
Washington, D. C. 20525

Dr. H. K. Doetsch
Arnold Engineering Development Center
Air Force Systems Command
Tullahoma, Tennessee 37389

Library
Air Force Rocket Propulsion Laboratory
(RPR)
Edwards, California 93523

Library
Bureau of Naval Weapons
Department of the Navy
Washington, D. C.

Library
Director (Code 6180)
U.S. Naval Research Laboratory
Washington, D. C. 20390

APRP (Library)
Air Force Aero Propulsion Laboratory
Research and Technology Division
Air Force Systems Command
United States Air Force
Wright-Patterson AFB, Ohio 45433

Technical Information Department
Aeronutronic Division of Philco Ford
Corporation
Ford Road
Newport Beach, California 92663

Library-Documents
Aerospace Corporation
2400 E. El Segundo Boulevard
Los Angeles, California 90045

Library
Bell Aerosystems, Inc.
Box 1
Buffalo, New York 14205

Report Library, Room 6A
Battelle Memorial Institute
505 King Avenue
Columbus, Ohio 43201

D. Suichu
General Electric Company
Flight Propulsion Laboratory Department
Cincinnati, Ohio 45215

Library
Ling-Temco-Vought Corporation
Post Office Box 5907
Dallas, Texas 75222

Marquardt Corporation
16555 Saticoy Street
Box 2013 - South Annex
Van Nuys, California 91409

P. F. Winternitz
New York University
University Heights
New York, New York

I. Forsten
Picatinny Arsenal
Dover, New Jersey 07801

R. Stiff
Propulsion Division
Aerojet-General Corporation
Post Office Box 15847
Sacramento, California 95803

Library, Department 596-306
Rocketdyne Division of Rockwell
North American Rockwell Inc.
6633 Canoga Avenue
Canoga Park, California 91304

Library
Stanford Research Institute
333 Ravenswood Avenue
Menlo Park, California 94025

Library
Susquehanna Corporation
Atlantic Research Division
Shirley Highway and Edsall Road
Alexandria, Virginia 22314

STL Tech. Lib. Doc. Acquisitions
TRW System Group
1 Space Park
Redondo Beach, California 90278

Dr. David Altman
United Aircraft Corporation
United Technology Center
Post Office Box 358
Sunnyvale, California 94088

Library
United Aircraft Corporation
Pratt and Whitney Division
Florida Research and Development
Center
Post Office Box 2691
West Palm Beach, Florida 33402

Library
Air Force Rocket Propulsion
Laboratory (RPM)
Edwards, California 93523

Allan Hribar, Assistant Professor
Post Office Box 5014
Tennessee Technological University
Cookeville, Tennessee 38501

NASA
Lewis Research Center
Attn: E. O. Bourke MS 500-209
21000 Brookpark Road
Cleveland, Ohio 44135

NASA
Lewis Research Center
Attn: D. L. Nored 500-203
21000 Brookpark Road
Cleveland, Ohio 44135

NASA
Lewis Research Center
Attn: G. E. DoWerth 500-313
21000 Brookpark Road
Cleveland, Ohio 44135

Princeton University
James Forrestal Campus Library
Attn: D. Harrje
Post Office Box 710
Princeton, New Jersey 08540

U.S. Naval Weapons Center
Attn: T. Inouye, Code 4581
China Lake, California 93555

Office of Naval Research
Navy Department
Attn: R. D. Jackel, 473
Washington, D. C. 20360

Air Force Aero Propulsion Laboratory
Attn: APTC Lt. M. Johnson
Wright Patterson AFB, Ohio 45433

Naval Underwater Systems Center
Energy Conversion Department
Attn: Dr. R. S. Lazar, Code TB 131
Newport, Rhose Island 02840

NASA
Langley Research Center
Attn: R. S. Levine, MS 213
Hampton, Virginia 23365

Aerojet General Corporation
Attn: J. M. McBride
Post Office Box 15847
Sacramento, California 95809

Colorado State University
Mechanical Engineering Department
Attn: C. E. Mitchell
Fort Collins, Colorado 80521

University of Wisconsin
Mechanical Engineering Department
Attn: P. S. Myers
1513 University Avenue
Madison, Wisconsin 53706

North American Rockwell Corporation
Rocketdyne Division
Attn: J. A. Nestlerode,
AC46 D/596-121
6633 Canoga Avenue
Canoga Park, California 91304

University of Michigan
Aerospace Engineering
Attn: J. A. Nicholls
Ann Arbor, Michigan 48104

Tulane University
Attn: J. C. O'Hare
6823 St. Charles Avenue
New Orleans, Louisiana 70118

University of California
Department of Chemical Engineering
Attn: A. K. Oppenheim
6161 Etcheverry Hall
Berkeley, California 94720

Army Ballistics Laboratories
Attn: J. R. Osborn
Aberdeen Proving Ground, Maryland 21005

Sacramento State College
School of Engineering
Attn: F. H. Reardon
6000 J. Street
Sacramento, California 95819

Purdue University
School of Mechanical Engineering
Attn: B. A. Reese
Lafayette, Indiana 47907

NASA
George C. Marshall Space Flight Center
Attn: R. J. Richmond, SNE-ASTN-PP
Huntsville, Alabama 35812

Jet Propulsion Laboratory
California Institute of Technology
Attn: J. H. Rupe
4800 Oak Grove Drive
Pasadena, California 91103

University of California
Mechanical Engineering Thermal Systems
Attn: Prof. R. Sawyer
Berkeley, California 94720

ARL (ARC)
Attn: K. Scheller
Wright Patterson AFB, Ohio 45433